UCLA
UCLA Electronic Theses and Dissertations

Title
Chemical Mechanical Polishing and Direct Bonding of YAG and Y2O3

Permalink
https://escholarship.org/uc/item/7zd130dt

Author
McKay, Jeffrey

Publication Date
2016

Peer reviewed|Thesis/dissertation

eScholarship.org Powered by the California Digital Library
University of California

UNIVERSITY OF CALIFORNIA

Los Angeles

Chemical Mechanical Polishing and Direct Bonding of YAG and Y_2O_3

A dissertation submitted in partial satisfaction

of the requirements for the degree of Doctor of Philosophy

in Materials Science and Engineering

by

Jeffrey Matthew Nicolas Mc Kay

2016

ABSTRACT OF THE DISSERTATION

Chemical Mechanical Polishing

and Direct Bonding of YAG and Y_2O_3

by

Jeffrey Mc Kay

Doctor of Philosophy in Materials Science and Engineering

University of California, Los Angeles 2016

Professor Mark S. Goorsky, Chair

Current limitations in both single crystal and polycrystalline (ceramic) solid state laser technologies for high power applications stem from thermal effects that cause degradation in both lasing efficiency and beam quality. YAG and Y_2O_3 have favorable material properties for producing these high power lasers. The objective of this dissertation was to formulate chemical mechanical polishing (CMP) processes for YAG and Y_2O_3 resulting in smooth surfaces, (< 1 nm RMS roughness), defect free, and subsequently suitable for direct bonding. The CMP process has been used in conjunction with surface activation to form YAG-YAG and Y_2O_3-Y_2O_3 bonded elements showing a proof of concept for the fabrication of composite laser elements. YAG single crystals

were successfully polished with a 70-nm colloidal silica solution containing NaOH (pH 9.9). X-ray photoelectron spectroscopy measurements provided insights to the chemical impact of the NaOH. After NaOH exposure, YAG showed complete removal of Al from tetrahedral sites and a change in the $Y_{3/2}$ and $Y_{5/2}$ peak area ratios, indicating that the surface of YAG was sufficiently modified to allow the silica particles to abrade the byproduct surface layer. The final surface roughness after polishing was measured at 0.1 nm RMS roughness with no scratches deeper than 0.3 nm. YAG single crystals were also polished with a 70-nm Al_2O_3 slurry containing NaOCl (pH 11.4), however AFM measurements showed that the surface produced, 0.5 nm RMS roughness with no scratches deeper than 6.0 nm, was not as good as polishing with the colloidal silica slurry which was attributed to the effect of the chemical action of NaOH with the YAG surface. Polishing polycrystalline Y_2O_3 required a slurry with less aggressive chemical reactions, so the NaOCl/Al_2O_3 slurry was used to successfully polish the substrates to RMS roughness values of 0.5 nm and scratches no deeper than 1.0 nm. Triple axis diffraction rocking curves and double crystal x-ray diffraction imaging were used to demonstrate that the CMP process also removed subsurface damage that was present in the as-supplied material. The triple axis technique was also successfully employed for the first time to demonstrate that the polycrystalline Y_2O_3 subsurface damage was also significant reduced after the CMP process.

After CMP and surface treatment, YAG-YAG and Y_2O_3-Y_2O_3 were bonded together and annealed at 1425 °C with no applied pressure. Cross section and plan view high resolution transmission electron images of the YAG-YAG bonded interface revealed a

defect free bonding interface. Light transmission measurements showed that 90% of the interface area was bonded at room temperature contact and was further strengthened with annealing at 1425 °C for 72 hours. These conditions possess a much lower thermal budget than those previously shown to be required to bond YAG without a CMP step. The CMP and surface treatment processes that have been developed are applicable towards the creation of solid state laser composite elements and enable further progress and development for high power laser applications.

The dissertation of Jeffrey Mc Kay is approved.

Bruce S. Dunn

Robin L. Garrell

Mark S. Goorsky, Committee Chair

University of California, Los Angeles

2016

Table of Contents

ABSTRACT OF THE DISSERTATION ii

List of Figures viii

List of Tables xii

Acknowledgements xiii

VITA xv

Chapter 1. Introduction to the Dissertation 1

1.1. Overview 1

1.2. Solid-State Laser Materials 1

1.3. Yttrium Aluminum Garnet (YAG) 2

1.4. Yttria (Y_2O_3) 4

1.5. Present Motivations 5

1.6. Dissertation Outline 9

Chapter 2. Background and Theory 10

2.1. Chemical Mechanical Polishing 10

2.1.1 Material Removal 12

2.2. Wafer Bonding 14

2.2.1 Wafer Bonding Requirements 15

2.2.2 Wafer Bonding Mechanisms 17

Chapter 3. Description of the Characterization Techniques 21

3.1. Introduction 21

3.2. Atomic Force Microscopy 22

3.3. Optical Microscopy 23

3.3. High Resolution X-ray Diffraction 24

3.4. X-ray Photoelectron Spectroscopy 25

3.5. Bonded Area Imaging 26

3.6. Transmission Electron Microscopy 27

Chapter 4. CMP of Single Crystal YAG 29

4.1. Introduction 29

4.2. Experimental Setup 29

4.3. Al_2O_3 Based Slurry CMP Experimental Results 30
4.3.1 AFM Characterization of the CMP process 30
4.3.2 AFM Characterization of the Cleaning Process 34
4.4. SiO_2 Based Slurry CMP Experimental Results 35
4.4.1 AFM Characterization of the CMP process 35
4.4.2 XRD Characterization of the CMP process 38
4.4.3 XPS Characterization of the CMP process 42
Chapter 5. CMP of Polycrystalline Y_2O_3 48
5.1. Introduction 48
5.2. Experimental Setup 48
5.3. Al_2O_3 CMP Experimental Results 50
5.3.1 Surface Morphology Characterization of the CMP process 50
5.3.2 AFM Characterization of the CMP process 53
5.3.3 XRD Characterization of the CMP process 58
Chapter 6. Microstructure Characterization of Bonded Structures 63
6.1. Introduction 63
6.2. Experimental Setup 63
6.3. Bonded Area 64
6.4. Interface Microstructure 66
Chapter 7. Future Work 69
7.1. Summary 69
7.2. Y_2O_3/Y_2O_3 Bonding Interface Characterization 69
7.3. Bond Strength Characterization 70
7.4. Optical Transmission Characterization 70
7.5. Heat Transfer Characterization 70
Bibliography 72

List of Figures

Figure 1.1 – Bonding interface schematic highlighting current problems of composite elements for laser application 7

Figure 2.1 – Schematic of the CMP process 10

Figure 2.2 – Mechanics of abrasive/surface contact based off of Liu's model 13

Figure 2.3 – Hydrogen bond formation when hydrophilic surfaces come into contact 17

Figure 2.4 – Covalent bonding of two surfaces, after annealing 18

Figure 3.1 – Diagram of the AFM basic operating principles 22

Figure 4.1 – Location of the AFM scan positions for each YAG substrate 29

Figure 4.2 – 40 µm x 40 µm AFM scan at the center position for a YAG substrate prior to polishing 30

Figure 4.3 - 5 µm x 5 µm AFM scan at the center position for a YAG substrate prior to polishing 31

Figure 4.4 - 5 µm x 5 µm AFM scan at the center position for a YAG substrate after polishing with Al_2O_3, RMS roughness 0.3 nm, 1 – 5 nm scratches, similar to as received state 32

Figure 4.5 - 40 µm x 40 µm AFM scan at the center position for a YAG substrate after SC-1 treatment for 10 minutes 34

Figure 4.6 - 40 µm x 40 µm AFM scan at the center position for a YAG substrate after polishing with SiO_2, RMS roughness 0.1 nm 36

Figure 4.7 - 40 µm x 40 µm AFM scan of a scratch introduced YAG substrate to measure material removal rate 37

Figure 4.8 – Scratch depth versus total polishing time, removal rate was found to be 0.3 nm / minute 39

Figure 4.9 - TAD omega scans of YAG (444) before and after CMP with $NaOH/SiO_2$ for 30 minutes 39

Figure 4.10 – Drawing of exaggeration of crystal mosaicity near the surface which cause diffuse scattering tails observed in Bragg reflections 40

Figure 4.11 - X-ray Diffraction Topography Imaging Setup 41

Figure 4.12 - Double crystal X-ray topographs (10 4 0 reflection; GI geometry) of a single crystal YAG wafer, before and after polishing with SiO_2/NaOH 45

Figure 4.13 - The deconvoluted Al 2p XPS spectra of YAG a) untreated b) treated with 30 minutes of NaOH 46

Figure 4.14 - The deconvoluted O 1s XPS spectra of YAG a) untreated b) treated with 30 minutes of NaOH 47

Figure 4.15 - The deconvoluted Y 3d XPS spectra of YAG a) untreated b) treated with 30 minutes of NaOH 49

Figure 5.1 – Mounting set up for polycrystalline Y_2O_3 polishing. The sample of interest is in the center 50

Figure 5.2 – Nomarski image for polycrystalline Y_2O_3 substrate as received, grain boundaries clearly present along with contamination of the surface 51

Figure 5.3 – Profilometer scan of the surface of polycrystalline Y_2O_3 substrate as received 52

Figure 5.4 – Microscope image for polycrystalline Y_2O_3 substrate after mechanically grinding on 1 μm diamond paper , scratches are present 53

Figure 5.5 – Profilometer scan of the surface of polycrystalline Y_2O_3 substrate after mechanically polishing on 1 μm diamond paper, and a single crystal YAG sample (offset for clarity) for reference 53

Figure 5.6 – Location of the AFM scan positions for each Y_2O_3 substrate 54

Figure 5.7 – 40 μm x 40 μm AFM scan at the center position for an Y_2O_3 substrate prior to CMP 54

Figure 5.8 – Optical microscope images of CMP processing Y_2O_3 with various parameters: a) Pad: Suba 500, 4 kPa, b) Pad: Suba 500, 20 kPa, c) Pad: Politex, 4 kPa, d) Pad: Politex, 20 kPa 56

Figure 5.9 – 40 μm x 40 μm AFM scan at the center position for an Y_2O_3 after 30 minutes of Al_2O_3/NaOCl CMP 57

Figure 5.10 – Double crystal diffraction powder scan of polycrystalline Y_2O_3 after 20 μm SiC lapping 58

Figure 5.11 – Double crystal diffraction rocking curve of polycrystalline Y_2O_3 (222) after 20 μm SiC lapping 59

Figure 5.12 – Polycrystalline Surface with (222) planes drawn, incident X-ray beam illuminates multiple grains at once, but only the grain marked by the star is in a diffracting angle 60

Figure 5.13 - TAD omega scans of Y_2O_3 (222) a) after 20 μm SiC lapping (FWHM 238") b) after 6 μm diamond lapping (FWHM 129") c) after 1 μm diamond lapping (FWHM 94") d) after Chemlox CMP FWHM(33") 61

Figure 6.1 – IR Images of YAG/YAG bonding (10 mm diameter) a) as bonded (room temp), b) annealed at 250 °C for 24 hours, c) annealed at 1425 °C for 72 hours 64

Figure 6.2 – IR Images of YAG/YAG bonding (10 mm diameter) with optimized polishing process (90% area bonded) a) as bonded (room temp), b) annealed at 250 °C for 24 hours, c) annealed at 1425 °C for 72 hours 65

Figure 6.3 – IR Image of Y_2O_3/Y_2O_3 bonding (10 mm diameter) with optimized polishing process after annealing at 1425 °C for 72 hours 66

Figure 6.4 – Cross section of bonded YAG/YAG interface after annealing. [023] Zone Axis 67

Figure 6.5 – Plan view of YAG/YAG interface after annealing. [111] Zone Axis 68

List of Tables

Table 1.1 : Physical and optical properties of Nd:YAG 2

Table 1.2 : Physical and optical properties of Nd:Y2O3 4

Table 4.1 TAD rocking curve breaths from Figure 4.9 40

Table 5.1 Compilation of TAD rocking curve FWHMs 62

Acknowledgements

I have spent over 9 years at UCLA during my undergraduate and graduate life and have met many people that have helped me along my Ph. D. journey. I would like to first thank Professor Bruce Dunn, Professor Garrell, and Professor Kodambaka for serving on my Ph. D. committee and providing me insightful and thoughtful discussions about my work. The chair of my committee, Professor Mark Goorsky, has been an excellent advisor and has provided me the tutelage to become a successful scientist.

I would further like to thank all of the UCLA Materials Science and Engineering faculty and staff. Our department truly displays a collaborative effort and vision I have worked with every one of our departments groups on various projects and was pleased with the support and dedication our students have for helping other's projects and experiments. Specifically I would like to thank Tze Bin-Song from Professor Yang Yang's group for providing the XPS measurements for this thesis.

I have made a list of lifelong friends at UCLA that helped me along and provided entertainment and relaxation other than spending long nights working on various research projects. All my group members were invaluable and have helped me in ways that they probably could not even imagine. Mike, Steven, Stanley, Xiaolu, Saurabh, David, King, Caroline, Chao, Mark, Brett, Tingyu, Sean, and many others have all been people that I felt confident in depending on and provided me with necessary help for my project to reach its fruition.

Finally I would like to thank my family. My mom and dad have provided me with support and have always been proud of the work I accomplished. I hope as I move into the next phase of my life, I will continue to make them proud. Lastly, I would like to thank my fiancée, Sherry, for all of her patience through the years and she helped me stay motivated and never let me stray off from my goal.

VITA

2010 Bachelor of Science in Materials Science and Engineering

University of California, Los Angeles

Los Angeles, CA

2012 Master of Science in Materials Science and Engineering

University of California, Los Angeles

Los Angeles, CA

PUBLICATIONS

Mc Kay, Jeffrey, Caroline Moulet-Ventosa, and M. S. Goorsky. "Chemical-Mechanical Polishing YAG For Wafer Bonding." ECS Transactions (2013)

Mc Kay, Jeffrey, Tingyu Bai, and M. S. Goorsky. "Development of Materials Integration for Laser Gain Media: Single Crystals and Ceramic (Polycrystalline) Materials and Applications." ECS Transactions (2014)

Mc Kay, Jeffrey and M.S. Goorsky. "Chemical Mechanical Polishing of III-V Materials for Wafer Bonding Applications." ECS Transactions (2014)

Mc Kay, Jeffrey and M.S. Goorsky. "Effects of Miscut Substrates on Electrical Conductivity Across InP and GaAs Wafer-Bonded Structures." ECS Transactions (2014)

Chapter 1. Introduction to the Dissertation

1.1. Overview

Light amplification by stimulated emission of radiation (LASER) is one of the greatest enabling technologies of the twentieth century. Lasing has been achieved with a wide variety of hosts in the form of solids, liquids, and gases. Specifically, the advancement of solid-state lasers (SSLs) since the invention of the first ruby laser has seen tremendous leaps in conversion efficiency and maximum output power. SSLs have many favorable material properties, such as high thermal conductivity, high chemical stability, mechanical durability, long operational lifetime, and versatile output characteristics (average and peak power, pulse width, repetitition rate, and wavelength) [1]. Many potential applications depend upon the ability to engineer new types of SSLs by synthesizing new host materials doped with various rare earth elements as the active ions, to generate desired optical parameters mentioned above and by integrating grown material into new types of structures. Significant progress has been made in applying SSL technology to diverse fields of study such as scientific research [2,3], medical [4,5], military [6,7], and commercial [8,9] applications. Further development into improving SSL technologies will provide benefit to all of the above areas.

1.2. Solid-State Laser Materials

SSLs have emerged as one of the most widely used lasing media and have been developed for many new applications, such as glass lasers in nuclear fusion reactors, mechanical processing, and medical applications [10]. SSLs can be made of either crystalline or non-crystalline materials. Common SSL media are made of hard and brittle

oxides such as Ruby, Yttrium Aluminum Garnet (YAG, $Y_3Al_5O_{12}$), Yttria (Y_2O_3), Sapphire (Al_2O_3), and Lithium Niobate ($LiNbO_3$) which are all common host materials. Doping these host materials with rare earth elements (Nd, Yb, Er) or transition metals (Cr^{+2} or Fe^{+2}) allows for emission of wavelengths ranging from UV to Mid-IR [11]. These materials exhibit high stiffness, high strength, and wear resistance therefore are typically prone to machining damage during growth and processing, which leads to these media to be vulnerable to brittle fracture. Thus when these SSL materials are subjected to high thermal stresses during operation, they tend to fail by crack propagation [12]. Since most applications use SSLs that are made from single crystal material, it is clear that improvement of materials processing is just as critical as the development of the crystal growth technology of these materials.

1.3. Yttrium Aluminum Garnet (YAG)

Single crystal YAG composes a majority of the SSL market, because it is a material that exhibits desirable characteristics for laser gain media (large cross-section of stimulated emission, long fluorescence lifetimes, low laser thresholds, and high energy conversion efficiencies) [13]. YAG is a colorless, optically isotropic crystal which has a garnet cubic structure. When doped with neodymium, for example, Nd:YAG crystals lase in the IR region at 1.06 μm. The wavelength emitted along with other important mechanical properties listed below in Table 1.1 [14] are all attractive properties for laser operation.

Table 1.1 : Physical and optical properties of Nd:YAG

Melting Point	1970 °C
Knoop Hardness	1215 kg/mm^2
Density	4.56 g/cm^3
Thermal Conductivity	12 W·m^{-1}K^{-1}
Coefficient of Thermal Expansion	8.2×10^{-6} °C^{-1}, 0–250 °C

Almost all of the YAG used to fabricate SSLs are single crystals. The boules were initially grown by the Verneuil process [15], but now the Czochralski process is typically used due to increases in laser amplification energy and laser beam quality [16]. YAG boules take a month or longer to grow and only contain a fraction of optically homogenous regions in the boule which are (regions are) suitable for use in an SSL (~60% area) due to intrinsic core and facets that form during growth [17]. This severely limits the fabrication of large dimension SSL, which in turn, constrains the design limits of high-powered SSLs.

Recent developments in ceramic technology have shown promise in the fabrication of polycrystalline ceramic laser materials. One of the largest problems with polycrystalline materials being used as a host material, is the issue of grain boundaries which disrupt the efficient amplification of the beam due to scattering. Successful laser oscillation from ceramics was first demonstrated in 1964 using Dy:CaF_2, but the initial results of a poor beam quality and lasing efficiency dissuaded any further development in

the field of ceramic laser media [18]. The field was reopened with renewed interest when Ikesue demonstrated a highly efficient polycrystalline Nd:YAG ceramic laser at room temperature in 1995 [19]. His work demonstrated that ceramic materials can possess lasing performances equivalent to that of single crystal material. Ceramic laser materials offer advantages in ease of fabrication, shape, size, and control of dopant concentrations, which were unable to be met through single crystal growth. Current state of the art ceramic laser material has optical quality that is comparable to high quality single crystal counterparts, and increased performance and potential applications are expected from further development in this technology.

1.4. Yttria (Y_2O_3)

Y_2O_3 is another material that has been studied and developed as a promising active host material, because of its favorable material properties such as a refractory nature, stability, and optical clarity over a large spectral range [20-23]. One important property of note is the thermal conductivity of Y_2O_3 is two times higher than YAG making it a more suitable candidate for high power (multi-kW) SSL applications [24]. However, it was only the advancement of ceramic laser technologies that led to Y_2O_3 as the host material , because single crystal Y_2O_3 has a high melting temperature (2430 °C) making it difficult and costly to grow large-sized Y_2O_3 single crystal boules, when compared to YAG for example. Ceramic Y_2O_3 fabrication and growth is a far easier task, as the sintering temperature necessary is “only” 1700 °C [25]. Studies in this area have led to the development of very successful sintering methods that are able to produced highly transparent Y_2O_3 ceramics that are suitable for laser oscillation [26]. Development

of ceramic laser technology has opened up new materials of interest (such as Y_2O_3, material properties as listed in Table 1.2 [27].) as next generation laser media.

Table 1.2 : Physical and optical properties of $Nd:Y_2O_3$

Melting Point	2430 °C
Knoop Hardness	940 kg/mm^2
Density	5.04 g/cm^3
Thermal Conductivity	17 $W \cdot m^{-1}K^{-1}$
Coefficient of Thermal Expansion	6-7 × 10^{-6} $°C^{-1}$, 0–250 °C

1.5. Present Motivations

Current laser media are typically fabricated from single crystals or glass of a uniform design and simple composition, which has served as the foundation of SSL research and applications in the twentieth century. Past research and efforts have been devoted to laser media, which has resulted in a constantly improving power output, beam quality, pulse generation time through research of amplifying the emission generated from these media [28]. Most of the research and development in this field has been focused on improving optical quality, producing larger dimension media, or growing single crystals with new compositions. These past techniques have now begun to reach their limitations in the performance that are able to be achieved in SSL technology. New laser structures have been designed to meet the demands for ever increasing output power and beam quality. One of these designs is called a composite laser element, which is

formed by bonding different media with two or more differing compositions. An example of a composite laser was first demonstrated in 1995 and realized increased levels of performance that could not be achieved by simple laser element designs [29].

The most common way to form these composite laser elements from single crystal materials is by first optically polishing the bonding surfaces to have very low RMS roughness (< 1 nm) and very high flatness. Previous works in literature have shown that for standard mechanical polishing (Al_2O_3 or diamond abrasives), it introduces subsurface damage that extends 1 μm into the substrate [76]. Removing the subsurface damage via etching has been shown by Marion to improve the mechanical fracture strength, but leaves the surface unusable for bonding [77]. Further studies have shown laser damage threshold tests to be improved by finer polishing methods [72]. There have been no published studies about the influence of CMP on the mechanical strength or lasing performance of YAG or Y_2O_3. The crystal surfaces are then brought into contact with each other under high temperature (~1600 °C) for long periods of time (> 100 hours), to undergo what is normally referred to as diffusion bonding [30]. This technique is capable of producing composite laser elements, but these composites an have several materials-related issues:

1. The orientations of the bonded crystals can be different from each other, leading to synthetic grain boundaries [31].

2. Current bonding processes are limited to bonding of flat surfaces and thus only simple design composites can be produced [32-33].

3. Surface roughness at the bonding interface forms interstices which result in poor thermomechanical properties in the composite element, which is not resistant to high power laser damage. 4. Subsurface damage introduced during lapping and mechanical polishing steps also reduce laser damage threshold by reducing the fracture strength, providing sites for light-absorbing contaminants to reside, and by causing atoms near the fracture surfaces to be easily ionizable [72].

5. The diffusion distance of laser active ions is limited, and it is not possible to control the microstructure of the bonding interface.

The largest issue stems from how these surfaces are initially polished. The surface roughness at the interface means only partially contacted points are generated during the bonding process as seen in Figure 1.1 [33].

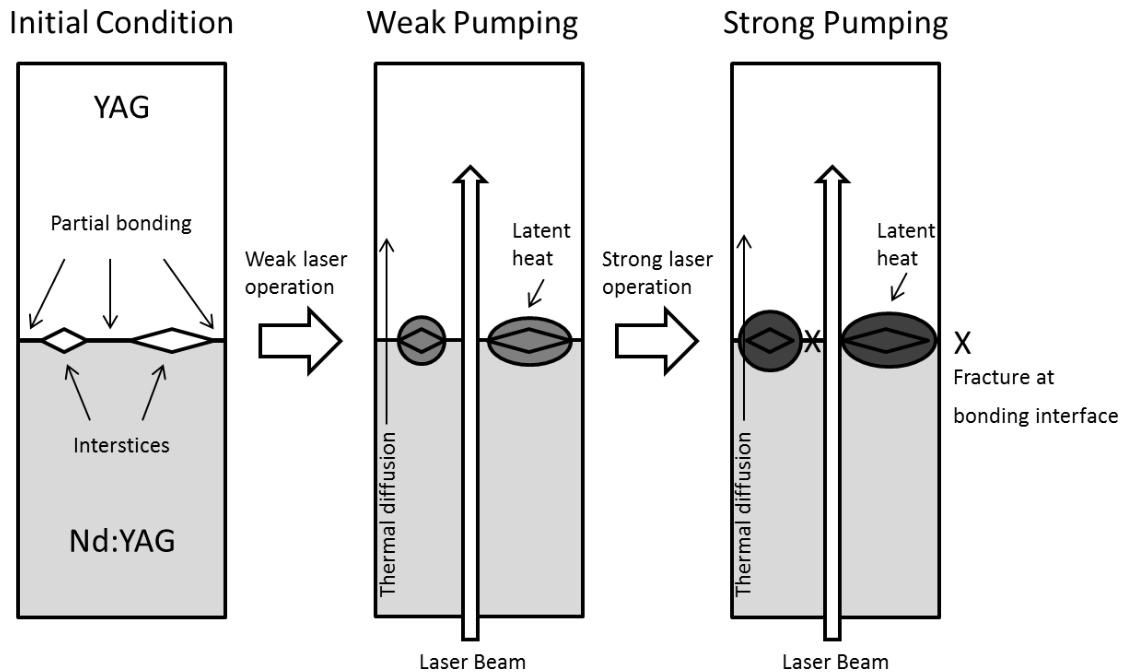

Figure 1.1 – Bonding interface schematic highlighting current problems of composite elements for laser application.

The defects at the interface absorb the thermal energy and as a result the beam quality and lasing efficiency decrease. In addition, the partial bonding and defects at the interface leads to low bond strength compared to the bulk strength of the starting materials, which prevents composite elements from being produced for industrial use.

In an effort to improve the bonding technology that is used to fabricate these composite elements, the study of the preparation of the surface of the material was a deemed critical component for successful bonding. It was found that the industry standard method of polishing YAG and Y_2O_3 left residual subsurface damage and defects on the surface. Chemical mechanical polishing was assessed for the preparation of the

surface of the lasing material. It was found that CMP was a technique that reduces the amount of subsurface damage and surface defects, resulting in increased performance and efficiencies in the development of composite laser elements. Once the surfaces were sufficiently prepared, bonded YAG-YAG and Y_2O_3-Y_2O_3 structures were created as a proof of concept and to study the properties of the bonded interface.

1.6. Dissertation Outline

In this thesis, the full process methodology of CMP and wafer bonding and the characterization of both are provided. Chapter 2 emphasizes the theories and models behind CMP and wafer bonding. Chapter 3 focuses on the characterization methods used in this study, including surface sensitive techniques for characterizing the CMP process and the bonding interface characterization for analyzing the bonding quality. Chapter 4 details the CMP processing conditions of single crystal YAG, including the characterization of the surface via atomic force microscopy (AFM), x-ray difraction (XRD), and x-ray photoelectron spectroscopy (XPS). Chapter 5 details the CMP processing conditions of polycrystalline Y_2O_3, including the characterization of the surface via AFM, XRD, optical microscopy, and surface profilometry. Chapter 6 details the bonding of the YAG/YAG and Y_2O_3/Y_2O_3 structures, including the bonding area evolution as a function of annealing, and the microstructure of the bonded interface of the YAG/YAG sample. Chapter 7 concludes the entirety of the work and proposes several ideas that should be accomplished in future works.

Chapter 2. Background and Theory

2.1. Chemical Mechanical Polishing

Chemical mechanical polishing (CMP) is one of the leading techniques in industrial and research environments to achieve both local and global planarization requirements, and is applicable to numerous materials (metals, semiconductors, oxides, etc.) [34]. CMP is one of the enabling techniques in fabricating functional optoelectronic materials, due to requirements of low surface roughness such that electromagnetic radiation can be transmitted or reflected at the surface without scattering loss by non-uniformities or defects at the surface. CMP is also able to produce damage-free surfaces without any residual strain which is an essential quality for materials to be used in high power lasing applications [28].

In the CMP process, the surface to be polished is pressed against a rotating polymer based pad while a slurry or combination of abrasives and chemicals are dispensed onto the pad, as shown in Figure 2.1.

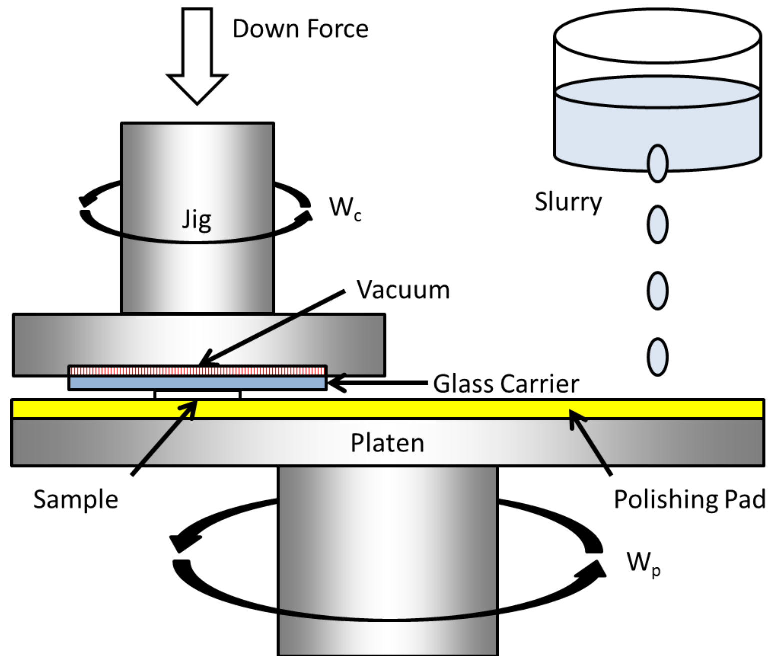

Figure 2.1 – Schematic of the CMP process

The platen (and polishing pad attached to it) rotates at a user designated speed typically measured in revolutions per minute (RPM), which is strongly correlated to the material removal rate. The jig sits on top of the polishing pad, which both holds the wafer and applies uniform force while pressing the wafer into the pad, so uniform removal occurs across the entire surface of the wafer. A chemical slurry consisting of abrasive particles and a mild corrosive (typically an oxidizer of the material to be polished) is dispensed onto the pad at a constant rate. The chemistry in the slurries is designed to react to the surface of the wafer and mechanically weaken it, which is then more easily abraded by the particles in the slurry leading to a smooth surface of high planarity. The desired CMP process will not promote the generation of brittle fractures on the sample surface, but will remove the surface by means of plastic deformation to produce a mirror finish [34].

There are many factors and variables involved in the CMP process, such as the abrasive material, abrasive size, chemistry of the slurry, type of pad, rotation speed, force, and etc. all of which will determine the polishing removal rate, surface roughness, defect concentration, and surface planarity.

What makes chemical mechanical polishing different from traditional polishing methods is the chemical action on the surface. In mechanical polishing, a harder material is used to scratch and chip away softer materials as a removal mechanism. This method tends to leave residual scratches on the surface (and subsurface damage) as will be seen later in Ch. 4. During the CMP process, the chemistry is chosen to modify the sample surface such that it becomes softer than the abrasive material and thus can be more easily abraded away than the pure substrate by mechanical action. Although the CMP process seems quite simple, achieving a more fundamental understanding has been limited due to the large number of variables for each polishing experimental design. These include the slurry (such as particle material, size, chemistry, pH, concentration, flow rate), pad (type, conditioning), tool (down pressure, linear velocity), and time-dependent contributions from the pad and slurry make the process difficult to understand and to control [34].

2.1.1 Material Removal

CMP uses slurry that has abrasives that are hard enough to remove the softer "modified" surface while leaving the harder substrate underneath the surface damage free. The removal mechanisms and model behind CMP was first developed by Preston [35]. He found that the removal rate was linearly dependent on the applied pressure and formed what is called the Prestonian model for CMP (Eq. 2.1).

$$\text{Material Removal Rate} = k_p \cdot V \cdot P \qquad \text{Eq. 2.1}$$

Here k_p is Preston's coefficient, V is the velocity, and P is the pressure. The Preston coefficient is used to combine the effects of surface chemistry, solution chemistry and abrasion. Conventional CMP models center around this approach, as the mechanical removal of material by abrasive particles is the major removal mechanism, but even with uniformly distributed pressure during polishing, there are experimentally observed removal rate changes from edge to center which are not apparent in Preston's model [36].

Numerous models have been proposed for material removal mechanisms during CMP to include friction-abrasion, mechanical removal, formation of reaction product film, and chemical dissolution. With these new models, it is presumed that the chemical action between the abrasives and surface enhance the mechanical removal and possible vice versa [37].

Liu's study of CMP of silicon, led to a modified version of Preston's model to include the chemistry, pad, sample, and abrasive parameters [38]. He proposed that the interaction between the abrasive particle and the wafer surface can be modeled as an elastic penetration of a spherical particle into the wafer surface with a uniform pressure P and sliding along with velocity V (Figure 2.2). This interaction helps disseminate the important parameters of the Preston's coefficient, and more describe in more detail the modified material removal rate equation (Eq. 2.2).

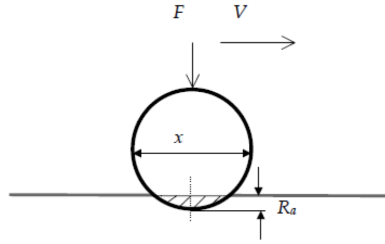

Figure 2.2 – Mechanics of abrasive/surface contact based off of Liu’s model

$$Removal\ Rate = C_e\left(\frac{H_w}{H_w + H_p}\right)\left(\frac{E_s + E_w}{E_s E_w}\right) * PV$$

where C_e is coefficient to account for chemical reactions, H_w is the hardness of the sample, H_p is the hardness of the pad, E_s is the Young’s modulus of the abrasive, and E_w is the Young’s modulus of the sample. With this model, there is a clear relationship between removal rate and processing parameters and can act as a guideline for the parameters to adjust for troubleshooting and gain insight into the smoothing rate of the surface.

2.2. Wafer Bonding

A second main objective of this thesis is to develop bonding techniques that are suitable for the fabrication of composite laser elements. The ability to create a bond that is both transmissive and has good thermomechanical properties is crucial to the feasibility of using composite elements for high power laser applications; therefore a thorough understanding of the mechanisms of bond formation between surfaces is necessary. Attributes of a successful bonding technique include large area uniform bonding, strong mechanical strength, and minimum increases in optical absorption. The requirements and

mechanisms for wafer bonding will be discussed in order to narrow the preferable processes to foster the successful bonding of these composite elements. Wafer bonding techniques have been shown to successfully bond together a large range of materials such as semiconductors (Si, GaAs, InP, etc.), metals, (Au, Ti, Cu, etc.) and oxides (SiO_2, Al_2O_3, YAG, Y_2O_3, etc) [39]. Successful bonding of all materials requires strict controls for the surface cleanliness, surface roughness, and surface flatness and that the chemical nature of the bonding mechanism is understood.

2.2.1 Wafer Bonding Requirements

Wafer bonding requires that the two surfaces to be bonded together possess a large surface area that can be intimately contacted. There are quantitative measurements that are used to determine whether the surfaces fall within the requirements for successful bonding. The surfaces curvature, measured in cm^{-1}, must be low as possible to allow maximum area contact without the need for excessive bonding pressures (which may damage/fracture the element). The total thickness variation (also known as 'flatness') , which is defined as the difference between the highest and lowest point of the surface, must also be minimized Lastly, the roughness of the surface, typically measured by an AFM, is given as the root mean square (RMS) deviation of the average height of the surface. Van der Waals bonding between the surfaces requires that areas on the surface are brought to less than 1 nm to the opposing surface, which requires the RMS roughness to be less than 1 nm [40].

Particle contamination on the surface will physically impede surfaces from bonding, leading to bubbles (microvoids) at the bonding interface. A model for sphere

shaped incompressible particles can be used to predict the bubbles radius based upon the theory of elastic deflection of thin plates and is given by Eq. 2.3 [39].

$$R_{bubble} \approx \frac{h^{1/2}}{\gamma^{1/4}} * [\frac{2Et_w^3}{3(1-\upsilon^2)}]^{1/4} \qquad \text{Eq. 2.3}$$

Where h is the particle radius, γ is the surface energy of the unbonded region, E is the Young's modulus, t_w is the thickness of each wafer, and ν is the Poisson's ratio. The predicted bubble radius for two YAG samples of 5 mm thickness with a bond strength energy of 0.25 mJ/cm^2 is 3.4 cm for a 100 nm sized particle (approximate size of slurry abrasive) [41]. It is clear that the presence of particles, especially leftover from the CMP slurry, will severely inhibit the bonding. In this study, the maximum starting radius of the samples was approximately 1.2 cm, so any particles on the surface will prevent bonding from occurring.

To minimize and eliminate the particles on the surface, the wafers undergo special cleaning treatments after CMP, which is discussed in Chapter 4. In addition, wafer bonding was carried out in a cleanroom environment, in which a constant downward laminar flow of filtered air will push down any airborne particles below the height at which bonding takes place. Even people in cleanroom attire will continuously shed particles, so it is important to minimize the surface exposure time between processing and handling steps that may contribute contaminants to the surface and prevent bonding.

2.2.2 Wafer Bonding Mechanisms

Current knowledge and research about wafer bonding mechanisms was mainly driven by the successful commercial adaptation of producing silicon on insulator substrates (SOI) via wafer bonding. The model that was proposed by Tan, Stengl, and Gösele for silicon bonding is the foundation for which most material bonding systems [42]. First, the bonding is classified as either hydrophobic (low polarity) or hydrophilic (polar) in nature. Hydrophobic surfaces are typically covered by a monolayer of hydrogen, which does not adhere well to polar water molecules. Hydrophilic surfaces are typically terminated by species of high electronegativity like a hydroxide or oxide which forms hydrogen bonds with the polar water molecules. This results in chemisorbed layers of water on the surface, which assists in the bonding process.

Formation of the hydrogen bonds is a three step process. The wafers to be bonded have a thin oxide on the surface, which react with water molecules forming X-OH on the surface. The bonding first occurs when the hydrophilic surfaces with adsorbed water are brought close together (< 1 nm) allowing the water molecules to form hydrogen bonds bringing the surfaces together (Figure 2.3).

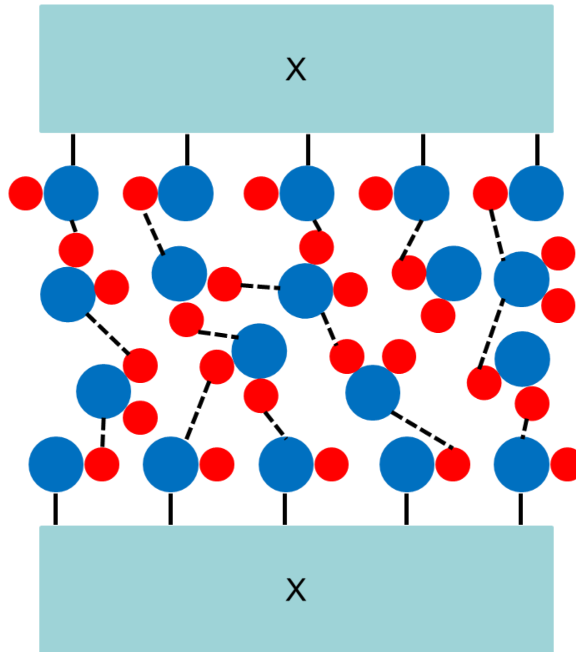

Figure 2.3 – Hydrogen bond formation when hydrophilic surfaces come into contact

The wafers are then heated so that the hydrogen bond bridges are shortened through the evaporation of water, thus bringing the wafers closer together. When the water evaporates, the interface bond becomes hydrogen bonding directly between surface groups [=X-OH – OH-X=]. Annealing the bond causes a condensation polymerization reaction to occur producing high strength covalent bonds (X-O-X) at the interface. Water is then able to diffuse out along the interface or into the bulk (Figure 2.4).

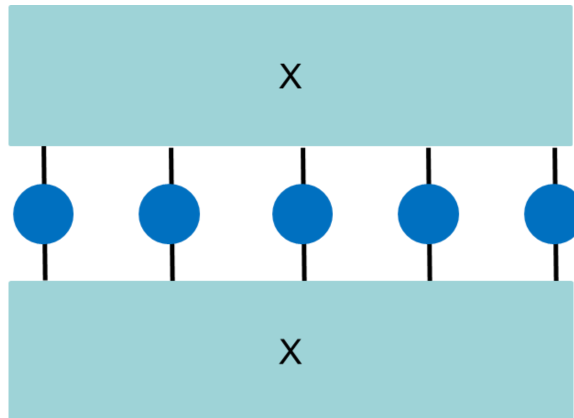

Figure 2.4 – Covalent bonding of two surfaces, after annealing

If the bonding surface is hydrophilic (surface terminated with hydroxyls –OH), then the surface there contain a few monolayers of water molecules. These water molecules are able to extend outwards via hydrogen bonding and form a bridge of water molecules across both surfaces (Figure 2.3). This fact allows for a relaxed surface roughness requirements for bonding, and can increase the bonding strength and the bonding yield. To strengthen the bond, heat treatments are typically performed in which the water by-products diffuse from the interface to the outside. Capillary forces bring the two surfaces into closer contact, such that direct chemical bonds can begin to form across the interface and the bonding energy can increase as high as the bulk strength of the material [43].

Since the van der Waals dispersion force is applicable to almost all substances in intimate contact, in theory, it is possible to be able to bond two solid plates of almost any material at room temperature given sufficiently flat and clean surfaces. In practice it is very difficult to achieve optically smooth and flat surfaces that meet the wafer bonding

requirements, so it would be very beneficial to create a reactive bonding surface to alleviate the surface smoothness requirements, by surface activation (making the surface hydrophilic). Some common silicon surface treatments that have been used for hydrophilic bonding are RCA1 (H_2O_2+NH_4OH+H_2O), RCA2 (H_2O_2+HCl+H_2O), and Piranha (H_2O_2+H_2SO4) [44]. It has also been shown that plasma treatments are also able to activate the Si surface, in which plasma treated surfaces are hydrophilic as well [45]. The background knowledge from Si surface treatments will be used as a basis for chemical and surface treatments to consider towards creating hydrophilic YAG and Y_2O_3 surfaces.

Chapter 3. Description of the Characterization Techniques

3.1. Introduction

CMP modifies the surface, so a combination of surface characterization techniques will provide a detailed study of the effects of CMP. Wafer bonding experiments will convert the surface into an interface, so characterization techniques for studying interfacial properties are performed. Atomic force microscopy (AFM) is extensively used in this study to measure the surface roughness and particle contamination after CMP processes. AFM will be used to determine whether the wafer surfaces are smooth enough after CMP. Optical microscopy is used to determine the initial surface flatness of the polycrystalline Y_2O_3 samples, as difference in the grain heights can easily be observed. Optical microscopy is also another quick method in order to check for particle contamination. High resolution X-ray diffraction (HRXRD) is used to determine the reduction of sub-surface damage that can be achieved by the CMP process. X-ray photoelectron spectroscopy (XPS) is used to determine the chemical state of the surface before and after exposure to the slurry chemistry. This will give insight to the surface modification during CMP and provide evidence for the polishing mechanism. When the bonded structures are fabricated, infrared imaging is used to measure the bonded area. To observe the interfacial microstructure, a focused ion beam (FIB) is used to create plan-view and cross-section transmission electron microscope (TEM) samples which are then imaged using a TEM. The following sections will briefly describe the operating principles of each of these characterization techniques.

3.2. Atomic Force Microscopy

Atomic force microscopy measures topographic features of the sample surface at a nanometer height scale, and thus is very good tool for measuring the surface roughness and cleanliness of the surfaces prior to bonding. The basic operation of an AFM is as follows and can be seen in Figure 3.1, there is a sharp tip (radius ~ 10 nm) on a cantilever that is attached to a piezoelectric. Scanning the sample involves the motor rastering the cantilever over the sample surface in an x-y pattern, during which the cantilever is oscillating near its resonant frequency. During oscillation, the tip begins to approach the surface morphology close enough that the van der Waals forces act on the cantilever which causes a decrease in the resonance frequency (as detected by a laser reflection and photodiode). The feedback loop in the system will adjust the height of the cantilever to maintain this constant resonance frequency and will record the height at that spot. By rastering across the sample area, a surface topography is generated at the end of the scan. The AFM software takes the surface topography map and calculates the root mean square (RMS) surface height roughness of the sample. Scans of multiple 40 µm x 40 µm areas (largest area possible on this system) are performed on sample surfaces using a Quesant Q-Scope 250 AFM to determine if the sample surface is clean (particle free) and smooth enough (< 1 nm RMS roughness) for wafer bonding purposes.

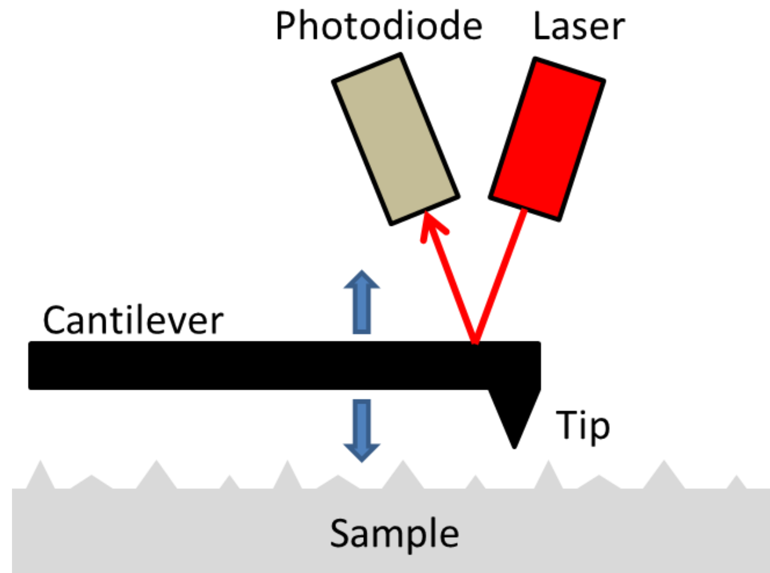

Figure 3.1 – Schematic diagram of an AFM

3.3. Optical Microscopy

Observation of the sample surface via optical microscopy technique is a complementary to AFM measurements in order to inspect large regions for particle contamination to determine wafer bonding feasibility. Whereas the AFM maximum scan area is a 40 µm x 40 µm and takes minutes to complete, optical microscopy is able to image much larger regions (2 mm x 2 mm) much quicker (seconds). In addition, optical microscopy is a useful tool in determining whether the grains on the surface of the polycrystalline Y_2O_3 are at the same height. Since the sample surfaces are usually a flat mirror polish, a microscope with differential interference contrast (DIC) is used to enhance the surface topography. The light source on the microscope passes through a birefringent Nomarski prism, which splits the beam into orthogonally polarized beams with small splitting angles and a relative phase shift. The beams then pass through the

objective lens and hit the sample surface. When the beams reflect off a flat area on the surface, they will be reflected and recombined in the prism in phase, producing an even contrasted image. When the beams reflect off slightly displaced areas of the surface, and are recombined by passing through the prism again, the beams will be out of phase during recombination and cause interference and contrast in that area of the image [46].

3.3. High Resolution X-ray Diffraction

High resolution X-ray diffraction is used to determine the reduction of subsurface damage before and after CMP of the samples. Manufacturing processes such as slicing, grinding, and lapping will introduce subsurface damage into the samples, which seen as microstructure changes, dislocations, and microcracks. X-ray diffraction is a useful non-destructive technique that is able to determine any lattice deformation of the crystal. The evaluation of subsurface damage can be accomplished by taking rocking curve measurements of strong diffraction peaks. Crystals with little or no subsurface damage will have a narrow FWHM indicating that periodic nature of the crystal is perfect or nearly perfect. Crystals with substantial subsurface damage will have a broader FWHM, which is caused by non-uniformities in the crystal by local expansion, contraction, or tilting of the crystal lattice [47-50].

For this work, HRXRD scans were taken on two different instruments. The first is a Bede D1 high-resolution diffractometer with a sealed copper x-ray tube source, a MaxFlux specular mirror to produce a parallel beam, which provided necessary intensity to characterize the polycrystalline Y_2O_3, a two bounce channel-cut (220) Si collimator

crystal to select Cu $K\alpha_1$ wavelengths (1.54056 Å), and a two bounce channel-cut (220) Si analyzer crystal. The second instrument is a Bede D3 high-resolution diffractometer with a sealed copper x-ray tube source, a (111) Si channel-cut collimator and a (220) Si analyzer crystal, which was used to characterize the single crystal YAG samples due to higher resolution.

3.4. X-ray Photoelectron Spectroscopy

X-ray photoelectron spectroscopy is used to examine the chemical state of the surface before and after exposure to the slurry chemistry to determine the material removal mechanism. During an XPS measurement, the surface is bombarded with monochromatic X-rays which are energetic enough to cause the ejection of core-shell electrons from the atoms at the surface. The ejected electrons will have a kinetic energy that is equal to the difference between the incident X-ray energy and the binding energy of the electron in that atomic core shell. The chemical species that is present on the sample can then be identified by matching the energies of the observed peaks to the National Institute of Standards and Technology X-ray Photoelectron Spectroscopy Database [51]. Quantification of the composition of the surface can be calculated by having adequate reference samples measured by the same tool.

The shapes of each photoemission peak provides information about the chemical bonding that occurs on the surface, as the differences in the electronegativities between various bonding species will cause core level chemical shifts in energy relative to known bulk peak energy positions. For example the binding energy of the Carbon 1s peak is 284.5 eV for bulk carbon, but additional peaks may appear at 285.9 eV if alcohol (C-O)

is present or at 287.3 eV if carbonyl (C=O) is present [52]. This information is useful for studying how the surface is modified by various chemical treatments, which can provide evidence for the material removal mechanism during CMP.

For this work, the XPS measurements were performed on an Omicron system with a base pressure of 10^{-9} or better, monochromatic Al Kα radiation (1486.6 eV), and a 20 eV band pass energy. The measurements were taken at a take-off angle of 20° between the surface and detector to enhance the signal from the bonding surface. The peak deconvolution was performed with the free XPSPEAK program and involved the subtraction of a Shirley background and curve fitting with a sum of 70% and 30% Gaussian and Lorentzian lines respectively.

3.5. Bonded Area Imaging

To measure the area of the bonding that occurs upon contact and further heat treatment, an infrared camera setup is used (a regular camera can also be used in this case, since some samples are transparent). In this setup, light is directed through the bonded sample to the camera. The bonded regions will appear in the images as areas with a uniform grayscale intensity level. Areas in which there is incomplete bonding, such as around particles or edges of the wafer, will show up as interference fringes due to the changes in index of refractions from the sample-air-sample interface. The grayscale intensity contrast will be periodic for every half wavelength change of the gap height, such that voids greater than 200 nm high can be imaged with lateral resolution of 0.5 mm [53]. These images can be further processed to calculate the percentage of the bonded area which is quantified by the number of pixels in the bonded region divided by the total

number of pixels of the sample area. This metric can be used to determine any changes in the bonding area that may occur with subsequent annealing processes.

3.6. Transmission Electron Microscopy

Transmission electron microscopy imaging allows for direct observation of the bonded interface to examine the microstructure. The TEM produces an electron beam that has a narrow energy and angular divergence via an electron gun and a series of magnetic lenses. This electron beam is focused onto a portion of a very thin (~100 nm) sample, which is electron transparent at this thickness. The sample is still able to scatter the electron beam, which results in a spatial distribution of the electron beam energy giving contrast to the image, which is recorded with CCD. In this simple description above, the image contrast will result from mass and thickness of the specimen, in which thicker or more massive regions of the sample will scatter more electrons and will appear 'dark' and the thinner or less massive regions of the sample will scatter less electrons and appear 'bright'.

In addition to mass-thickness contrast, another main contrast mechanism is diffraction contrast that arises since the wavelength of electrons in the beam are much smaller than the distances between atoms, diffraction occurs due to the periodic nature of a crystal. The incident electron beam is therefore split into the transmitted beam and multiple diffracted beams that are deflected by small angles determined by electron energy, crystal orientation, and lattice parameters. The diffraction pattern produced can be used as a guide for orientating the sample while inside the TEM, which is important for producing high resolution TEM images. When the sample is correctly oriented along

a major zone-axis, and a high magnification image is formed, it is possible to resolve the lattice fringes resulting from the phase contrast between each diffracted and transmitted beam. The resulting HRTEM image will appear to be an atomic resolution image of atoms in the actual crystal, but is not actually correct since the location of each fringe does not necessarily correspond to the location of the plane of atoms [54]. HRTEM is a very powerful technique for observing the crystal structure of the bonded interface and the orientation of the crystals at the bonded interface. The lattice imaging described above will allow for the observation of defects that may appear in the interface.

The samples for this study were first prepared by cutting the bonded structures with a wire saw using a SiC slurry. The (now) exposed bonded interface was then mechanically polished with diamond paper. A NOVA 600 Focused Ion Beam tool was used to extract cross section and plan view samples of the bonded interface via a Ga^+ source. The HRTEM images were taken on a FEI Titan TEM at an accelerating voltage of 300 kV.

Chapter 4. CMP of Single Crystal YAG

4.1. Introduction

In order to prepare YAG for wafer bonding experiments, the surface must first meet the smoothness requirements for wafer bonding (< 1 nm RMS roughness). A CMP process was developed which successfully brought the YAG surface roughness to acceptable values (< 1 nm RMS), removed scratches from the surface, reduced subsurface damage from prior polishing steps, and maintained a surface devoid of particles. This CMP process was characterized by AFM, XRD, and XPS in order to assess its effectiveness over traditional polishing steps.

4.2. Experimental Setup

Commercially purchased undoped 12.5 mm and 25 mm diameter (111) YAG substrates were used in all experiments. A Logitech PM5 CMP tool was used for all polishing and cleaning steps. The pads used in this study were a harder Suba 500 polishing pad (Shore D 55) and a softer Politex II polishing pad (Shore D 25).. The slurries used in this experiment were commercially available 70-nm SiO_2 suspension in a NaOH (4-6%) solution (pH 9.9) and a 70-nm Al_2O_3 suspension in a NaOCl (4-6%) solution (pH 11.4). Samples were polished at 30 minute intervals with a slurry flow rate of 5 mL / min and rotational speed of 35 RPM with a constant pressure of 20 kPa. The samples were attached to a glass carrier with wax, which was then held to the polishing jig via vacuum. Fiducial surface marks were also intentionally introduced prior to CMP in one of the samples to quantify the removal rate. After polishing, a 10 minute cleaning step was performed to remove any abrasive particles which would adhere to the surface.

First the tool was rinsed with deionized (DI) water to remove any remaining slurry. The polishing pad was then switched with a pad that has not been exposed to slurry. Samples were then cleaned with two solutions kept separated prior to mixing on the pad: a solution with a NaOCl to water ratio of 1:10 and a solution with a citric acid ($C_6H_8O_7$) to water ratio of 1:2 for 5 minutes. A commercial surfactant, Rodelene, was then added to the pad and flushed with DI water for an additional 5 minutes. Pressure and rotation speed were maintained for the cleaning step. After cleaning, the surface morphologies (40 μm x 40 μm scans) were measured with atomic force microscopy (AFM) to determine suitability of sample for wafer bonding.

4.3. Al_2O_3 Based Slurry CMP Experimental Results

4.3.1 AFM Characterization of the CMP process

Initial AFM scans of YAG substrates were taken prior to being subjected to CMP in order to determine the starting surface quality. All substrates had 40 μm x 40 μm scans taken in 5 positions denoted by Figure 4.1 in order to detect non-uniformity during polishing.

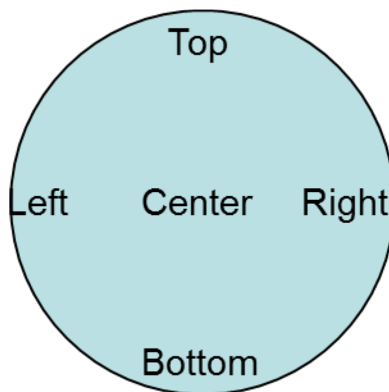

Figure 4.1 – Location of the AFM scan positions for each YAG substrate

An example scan prior to polishing taken from the center position of a YAG sample is shown in Figure 4.2, which shows the presence of scratches and particles on the surface. The average RMS roughness values from the YAG substrates prior to polishing were 1 – 4 nm. In Figure 4.2 there is a small square box within the scan, this demarks an area in which an even finer scan (5 μm x 5 μm) was taken, which is shown in Figure 4.3.

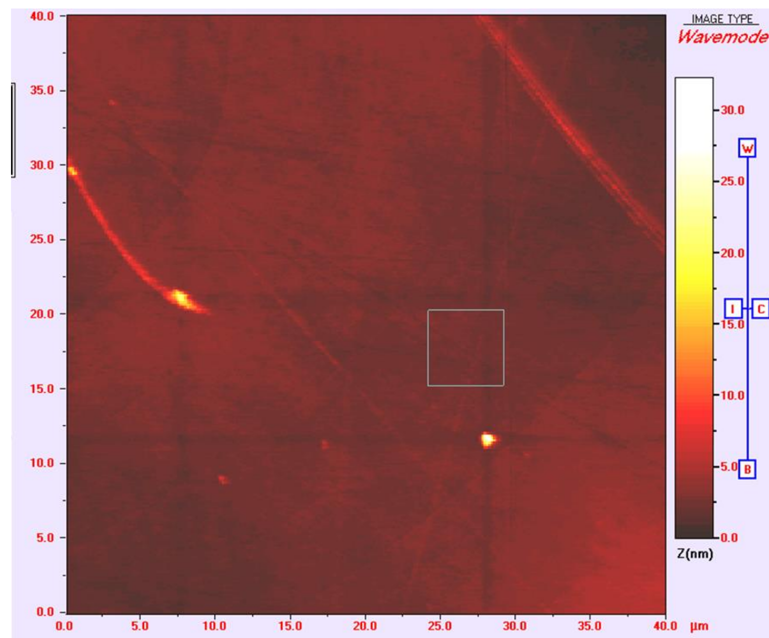

Figure 4.2 – 40 μm x 40 μm AFM scan at the center position for a YAG substrate prior to polishing

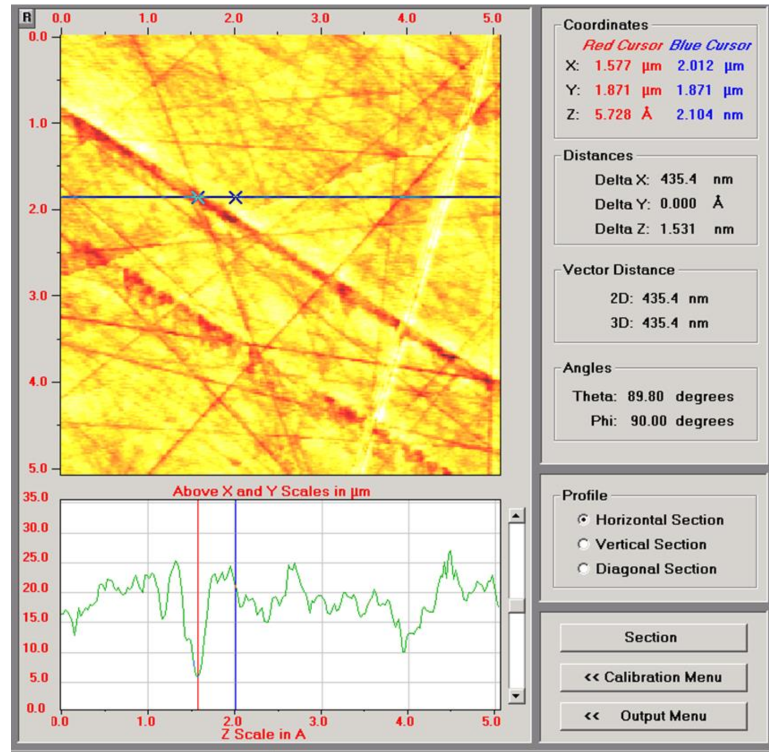

Figure 4.3 - 5 µm x 5 µm AFM scan at the center position for a YAG substrate prior to polishing

In Figure 4.3, the finer scan reveals the surface conditions of the samples much more clearly, in which it is covered in scratches from 1 – 6 nm in depth (presumably through commercial polishing steps) and a surface roughness of 1.0 nm. Initial AFM measurements showed that none of the samples received met the strict requirements of wafer bonding (< 1 nm RMS roughness and a particle-free surface).

The sample was then polished with Al_2O_3 in a NaOCl solution via the methodology outlined in the experimental setup section and measured again by AFM. Figure 4.4 shows the 5 µm x 5 µm scan after polishing for 30 minutes, in which the

measured surface roughness is 0.3 nm. Numerous scratches from 1-6 nm remain on the surface, which is common when using abrasives harder than the polished material [55]. Polishing the YAG an additional 30 minutes yielded similar surfaces (0.3 – 0.5 nm RMS roughness, 1-6 nm scratches), indicating the slurry is predominantly polishing the surface mechanically, in which surfaces free from subsurface damage will not be obtained. AFM showed no evidence that Al_2O_3 in NaOCl slurry improved the single crystal YAG surface after polishing, so we moved onto a different slurry for CMP. .

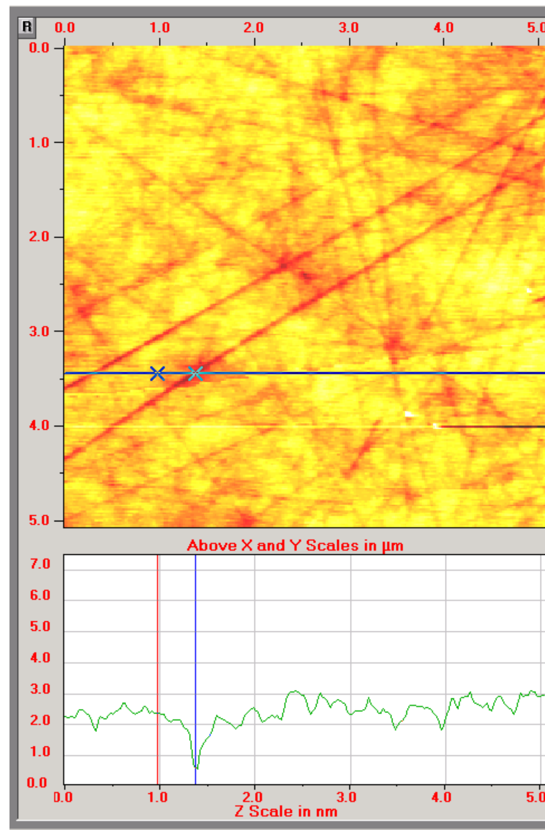

Figure 4.4 - 5 µm x 5 µm AFM scan at the center position for a YAG substrate after polishing with Al_2O_3, RMS roughness 0.3 nm, 1 – 5 nm scratches, similar to as received state

4.3.2 AFM Characterization of the Cleaning Process

The first experiment in post CMP cleaning is taken from the semiconductor industry and is called a Standard Clean-1 or SC-1, which is a heated solution of deionized water, ammonium hydroxide, and hydrogen peroxide [56]. This solution is typically used to remove any organic residue and particles that may exist on the surface of silicon and other semiconductor materials, however no literature has reported on its use on cleaning YAG surfaces. More specifically, the solution is composed of 1:1:5 ratio of $NH_4OH:H_2O_2:H_2O$, in which the NH_4OH and H_2O are first heated to 75 °C, then the H_2O_2 is added in, and the sample is immersed for 10 minutes. The AFM result from this treatment is shown in Figure 4.5, which had an RMS roughness of 15.2 nm.

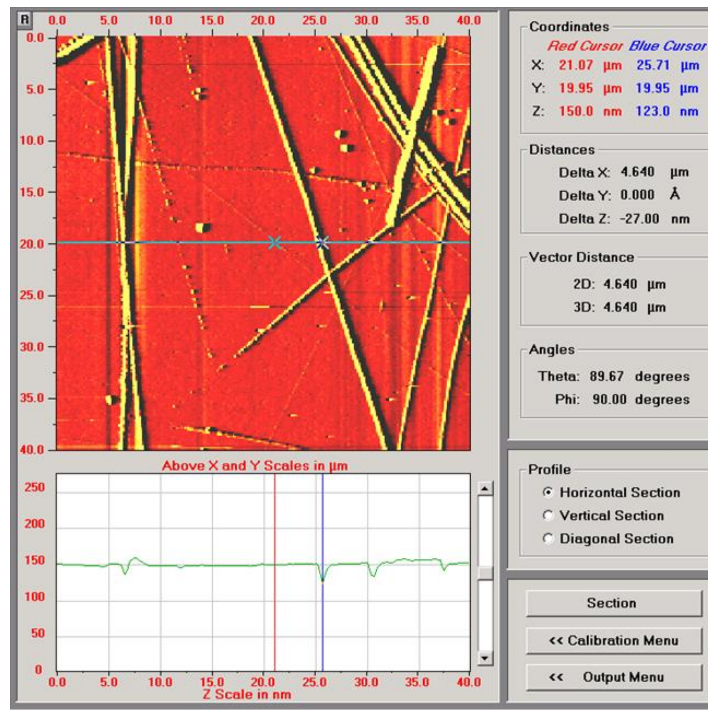

Figure 4.5 - 40 µm x 40 µm AFM scan at the center position for a YAG substrate after SC-1 treatment for 10 minutes

The increase of the RMS roughness can be attributed to the depth of scratches increasing from 1 - 6 nm to 20 - 60 nm. The increase in scratch depth was thought that SC-1 may act as some defect revealing etch for YAG, but this interesting result was not pursued, as it was detrimental to the main purpose of this study. In addition to the deeper scratches now present on the surface, there are still particles that remain on the surface, showing that this cleaning process was ineffective at improving the surface conditions of the YAG samples.

4.4. SiO_2 Based Slurry CMP Experimental Results

4.4.1 AFM Characterization of the CMP process

A new set of samples were used that had not been exposed to the Al_2O_3 slurry for this set of experiments, in which the samples were polished with a SiO_2 slurry suspension in a NaOH solution. Similar AFM scans of YAG substrates were taken prior to being subjected to CMP in order to determine the starting surface quality as seen in Figure 4.2. All substrates were similar in nature with RMS roughness measurements of 1 – 4 nm and scratches ranging from 1 – 6 nm in depth. The samples were polished with the methods explained in the experimental set up section and AFM results were recorded. Figure 4.6 shows the AFM scan after polishing, the sample had a measured RMS roughness of 0.1 nm with some scratches still remaining with depths of less than < 0.3 nm. The surface is also devoid of particles after the CMP cleaning process, without the need for any post-CMP type cleaning. The SiO_2 slurry was clearly more effective at producing the desired surfaces for wafer bonding applications.

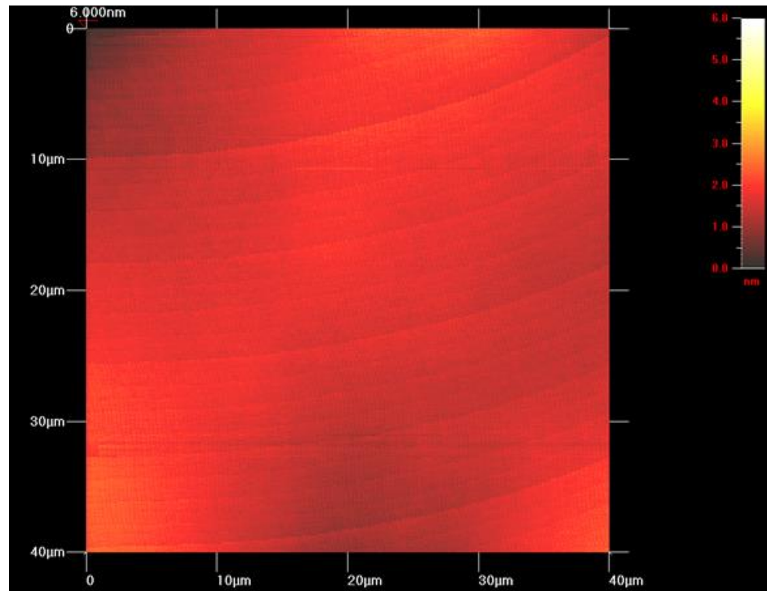

Figure 4.6 - 40 µm x 40 µm AFM scan at the center position for a YAG substrate after polishing with SiO_2, RMS roughness 0.1 nm

Large scratches were introduced onto a YAG wafer via a diamond scribe, and the depth was measured by AFM to determine the total removal rate of the CMP process seen in Figure 4.7. By measuring the change of scratch depth as a function of total CMP time, over 60 minutes, the overall average removal rate was found to be 0.3 nm / min which is shown in Figure 4.8. By polishing with a slow removal rate, the amount of material lost is minimal and scratches can be completely removed from the surface.

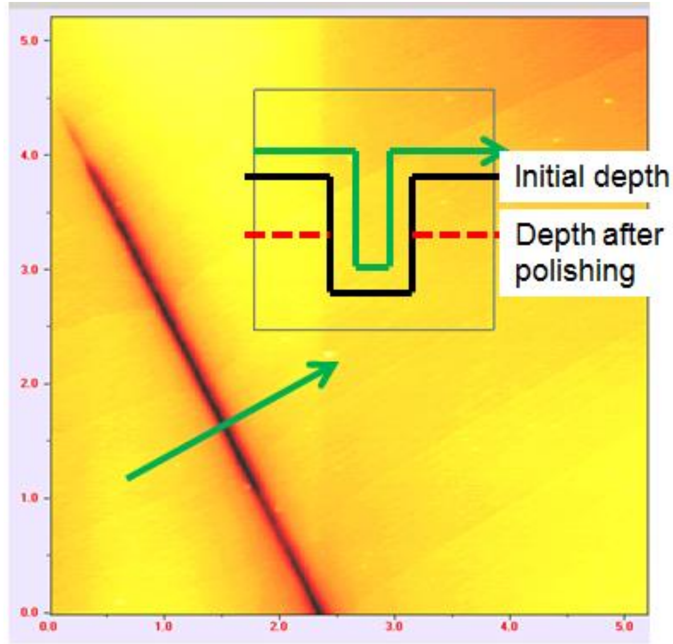

Figure 4.7 - 40 µm x 40 µm AFM scan of a scratch introduced YAG substrate to measure material removal rate

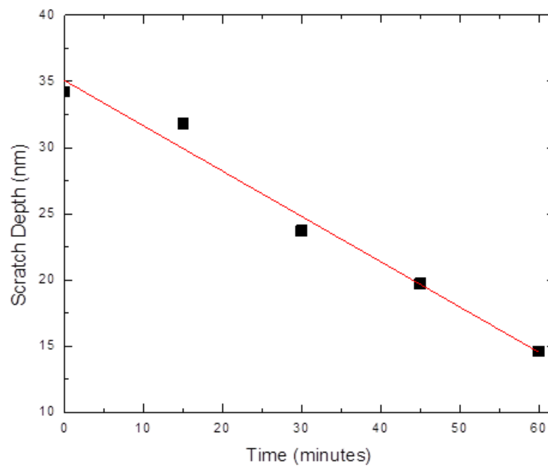

Figure 4.8 – Scratch depth versus total polishing time, removal rate was found to be 0.3 nm / minute

4.4.2 XRD Characterization of the CMP process

YAG substrates can have surfaces unsuitable for high power laser applications dependent on post-growth processing [64, 65]. The typical surface finishing these materials receive is a mechanical polish with Al_2O_3 or diamond, which leaves microscratches and residual subsurface damage. Therefore, CMP was also utilized to remove any subsurface damage that was introduced during the wafering process. This remaining subsurface damage limits the fracture strength, and ultimately the amount of power the laser material can handle [66].

The presence of subsurface crystalline damage was measured with triple axis x-ray diffraction (TAD) on a Bede D3 diffractometer[49, 67]. The instrumental broadening is only ~3 arcsec with negligible low intensity tails, giving resolution sufficient to observe changes in diffuse scatter in triple axis diffraction rocking curves of (444) [50, 68].

Figure 4.9 shows TAD omega scans of the (444) reflection of YAG before and after a 30 minute CMP run. Variation in the scan only begins to occur at the low intensity tails of the peak. The full width of the peak at 1/100 of the maximum intensity is sensitive to small disruptions of the crystal structure especially adjacent to the surface as seen in Figure 4.10. The FWHM, FW0.1M, FW0.01M, and FW0.001M for one of the samples are shown in Table 4.1 for comparison. The most noticeable aspect of these measurements showed that all of the CMP trials resulted in a smaller FW0.001M, indicating the reduction of sub-surface damage to the samples.

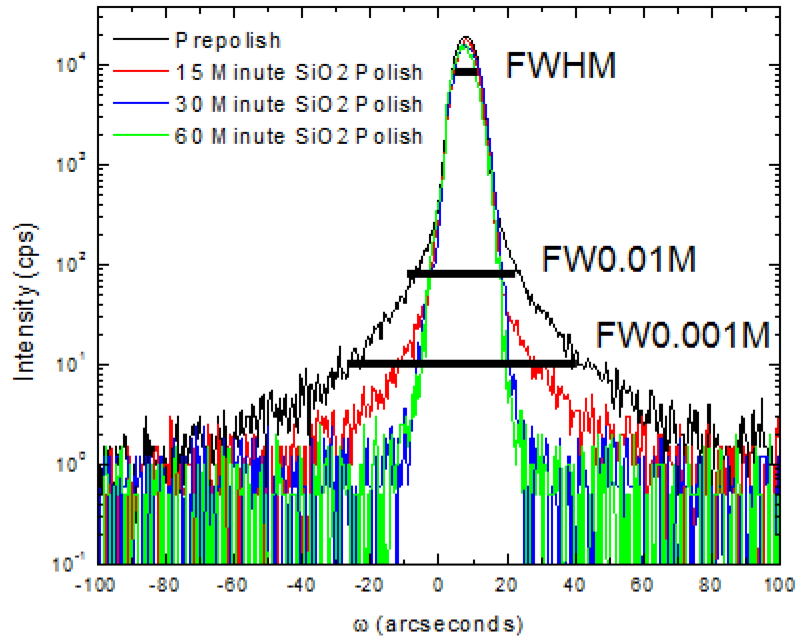

Figure 4.9 - TAD omega scans of YAG (444) before and after CMP with NaOH/SiO_2 for 30 minutes.

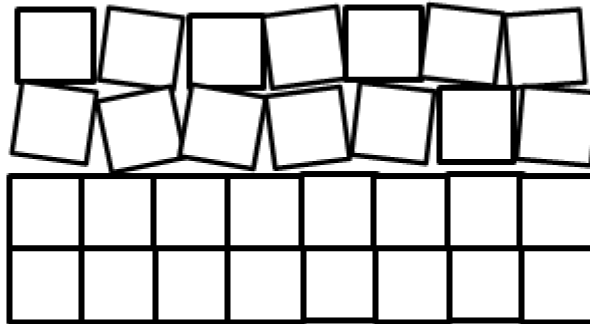

Figure 4.10 – Drawing of exaggeration of crystal mosaicity near the surface which cause diffuse scattering tails observed in Bragg reflections

TABLE 4.1 TAD rocking curve breaths from Figure 4.9

	FWHM [“]	FW0.1M [“]	FW0.01M[“]	FW0.001M [“]	Area under peak [“]
Prepolish	8	15	28	74	150,000
15 minutes	8	14	19	31	138,000
60 minutes	8	14	19	24	130,000

X-ray topography (XRT) is another technique to image the subsurface damage of our samples to compliment the rocking curves [69]. In the experimental setup, seen in Figure 4.11, the x-ray beam diffracts from a Si 224 crystal which expands the incident beam to a 3 by 5 inches beam.

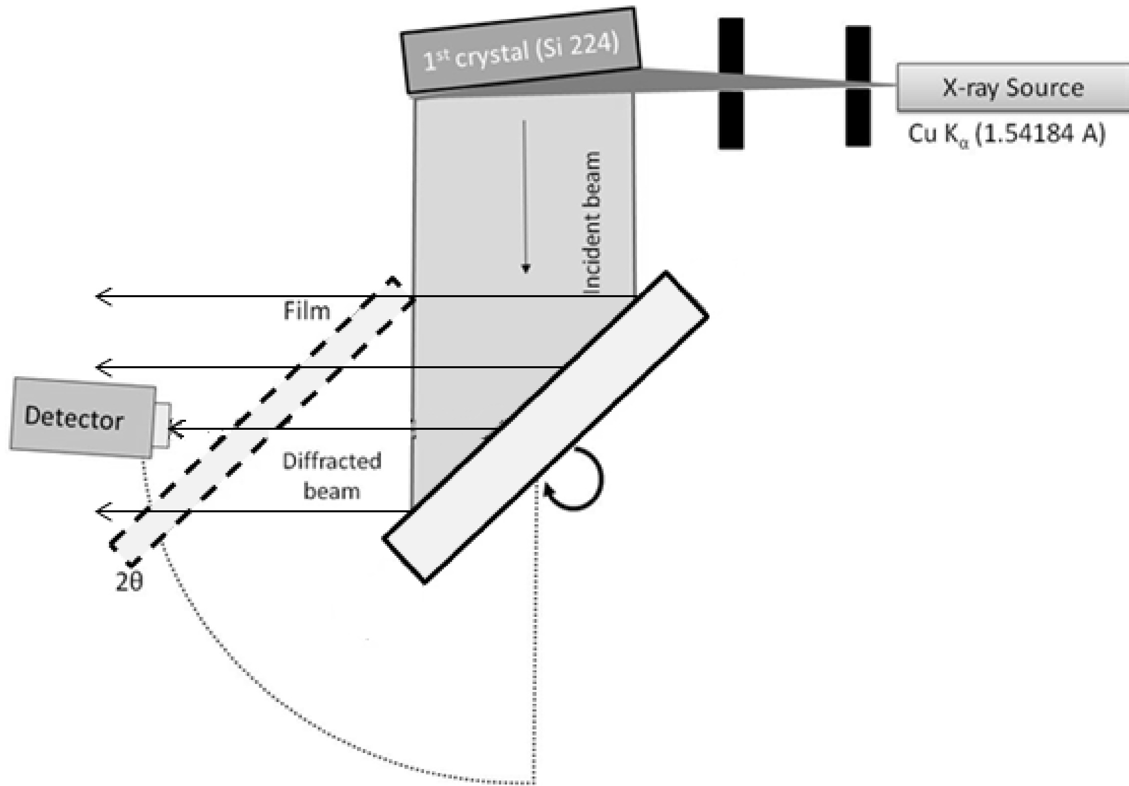

Figure 4.11 - X-ray Diffraction Topography Imaging Setup

This incident beam then diffracts off our YAG sample that is positioned at the glancing incident (10 4 0) Bragg angle. The diffracted beam then passes through an x-ray sensitive film, which images the diffracting regions on the surface shown in Figure 4.12. XRT was used to extract information from the subsurface layer. Subsurface damage leads to local strain and deformation, which gives diffraction contrast in the images.

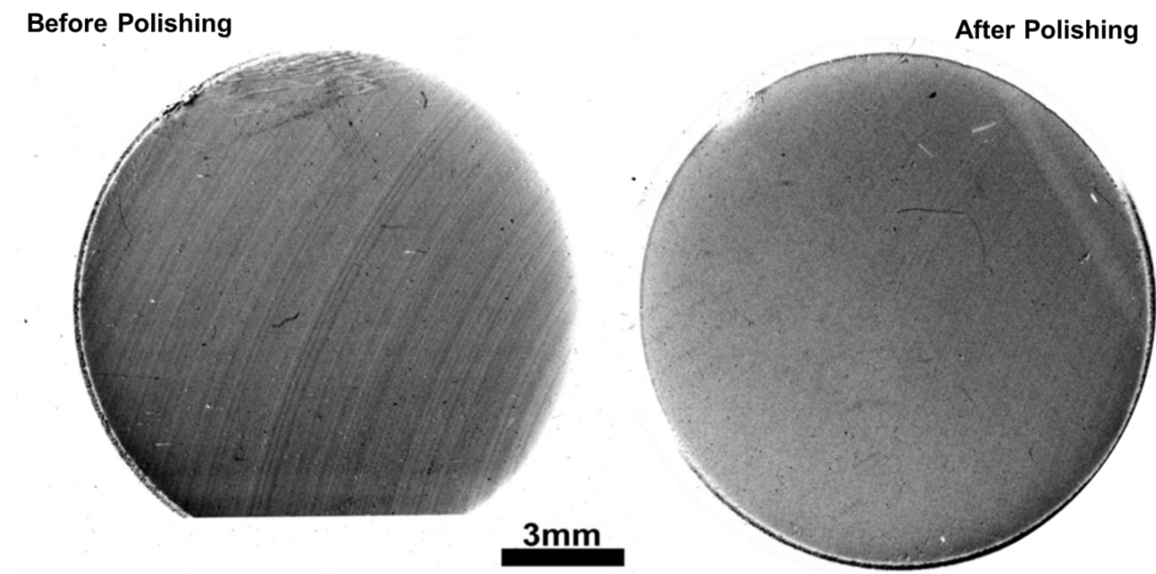

Figure 4.12 - Double crystal X-ray topographs (10 4 0 reflection; GI geometry) of a single crystal YAG wafer, before and after polishing with SiO_2/NaOH

On the left side of Figure 4.12, there is clear diffraction contrast from the sample that arises from sub-surface damage from the wafer slicing and intial polishing steps performed prior to our polishing steps. On the right hand side, the same YAG sample after SiO_2 polishing is imaged and exhibits a reduced diffraction contrast indicating a significant reduction in sub-surface damage, which complements the previous rocking curve data.

The correlation between fracture strength and subsurface damage has not yet been investigated in this study, but it is of interest for determining whether X-ray diffraction as non-destructive method to measure mechanical properties of these materials. The CMP process was found to also reduce subsurface crystalline damage in YAG as indicated by x-ray rocking curves reduction in FWXM. X-ray topography images showed a reduction of diffraction contrast after polishing which corroborates a reduction in subsurface damage for the YAG sample. CMP has been shown to improve the crystalline quality over previous surface preparation techniques used on the substrates and can be a pathway for further development and improvement of these materials for lasing applications.

4.4.3 XPS Characterization of the CMP process

YAG is a very hard and brittle material that is difficult to polish. The purely mechanical finishing techniques common in industry utilize hard abrasives such as diamond or Al_2O_3 and tend to leave scratches on the surface and residual subsurface damage. CMP is an approach that utilizes chemical reactions to modify the surface which can then be abraded away by softer abrasives such as SiO_2 to achieve the necessary global and local planarization that is required for wafer bonding [73, 74], 7). The slurry plays an important role in the CMP process, because it is an enabler for both the chemical and mechanical removal mechanisms. However, the mechanism of YAG polishing during CMP is not yet well understood and the author has found no published literature on the subject. The present investigation is designed to study the CMP characteristics of YAG in a basic NaOH solution and propose a removal mechanism based upon X-ray photoelectron spectroscopy (XPS) measurements.

In order to understand the effects of the slurry chemical reactions on the surface of the YAG, the variations of chemical composition of the surface was analyzed XPS measurements. Two samples were prepared, the first sample was prepared by mechanical polishing with a 1 μm diamond film and cleaned with deionized water and N_2 dried. The second sample underwent the same polishing conditions and then was immersed in a 5% NaOH solution at room temperature for 30 minutes to simulate the slurry chemistry during CMP. The sample was then rinsed with deionized water and dried with N_2. Both samples were transferred immediately to the XPS chamber after N_2 drying. Surface characterization was performed using a monochromatic Al kα (1486.6 eV) and 20 eV band pass energy. XPS measurements were taken at a 20° take-off angle between the surface and the detector to enhance the signal from the surface. Aluminum 2p, Oxygen 1s, and Yttrium 3d spectra were analyzed for the presence of core level chemical shifts. A neutralizer was used to eliminate charging in the non-conductive samples. Peak shifts were removed by shifting the spectrum to the Carbon 1s peak located at 285 eV and normalized by dividing spectrum intensity by the max intensity of the C 1s peak [80]. Peak deconvolution was achieved using with XPSPEAK program, utilizing curve fitting with a sum of 70% Gaussian and 30% Lorentzian lines.

While investigating this polishing process, it was first thought that SiO_2 abrasives should not be able to abrade the YAG surface because the hardness of SiO_2 is much lower than that of YAG (7 vs 8.5 on Mohr's scale). However, from the AFM measurements it is clear that the surface is indeed being polished by the NaOH/SiO_2 slurry. Therefore there must be some chemical reaction at the surface of the YAG, that

enables mechanical polishing to occur and it is this reaction that is important in controlling the final surface finish for CMP of YAG. To determine the chemical action on the surface, XPS spectra was collected from samples of YAG that were taken prior to the CMP step and one that was treated with a NaOH solution for 30 minutes.

Figure 4.13 shows the high resolution Al 2p spectra for the untreated and NaOH treated YAG after background subtraction and deconvolution of the peaks. For the untreated sample, the Al 2p lines are deconvoluted into two peaks centered at 73.1 eV and 74.8 eV. Based upon previous studies, this splitting has been identified due to two crystallographically nonequivalent aluminum ions identified in the garnet structure. Based on the garnet structure, it has been ascribed that the Al 2p signal at the lower binding energy corresponds to Al cations located at tetrahedral sites and the signal at the higher binding energy corresponds to Al cations located at the octahedral sites [78]. The NaOH treated YAG spectra lacks the lower binding energy line indicating, the selective removal of Al cations from the tetrahedral sites. This suggests that there is some chemical reaction occurring that is consistently removing aluminum from the surface.

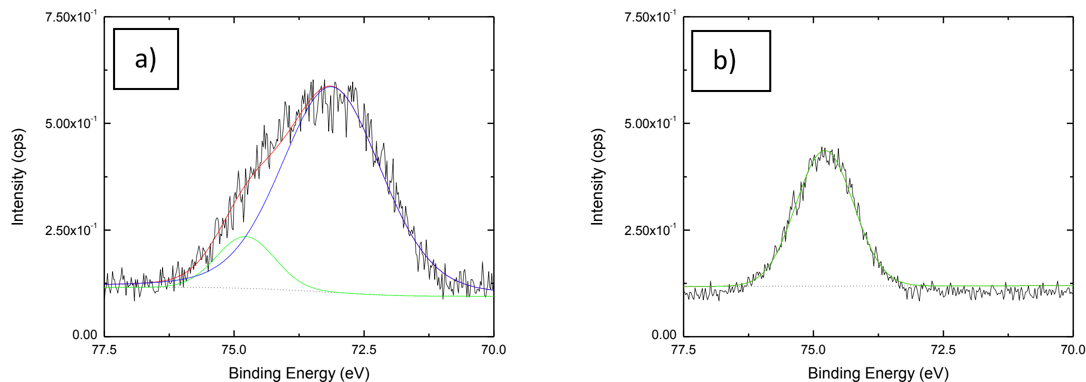

Figure 4.13 - The deconvoluted Al 2p XPS spectra of YAG a) untreated b) treated with 30 minutes of NaOH

Figure 4.14 shows the high resolution O 1s spectra for the YAG samples. For the untreated YAG, the O 1s lines have been deconvoluted into three lines with energies of 529.2 eV, 530.6 eV, and 532.2 eV. The peak at 529.2 eV is associated with Y-O bonds, peak at 530.6 eV is associated with Al-O bonds, and the peak at 532.2 eV is ascribed to either C=O or C-OH formed on the surface due to water absorbed by the surface [79]. The NaOH treated spectra only has two peaks, in which the density of Y-O bonds has increased relative to the number of Al-O bonds (from ~1/2 to nearly 1/1), which confirms that aluminum is preferentially removed from the surface during exposure to NaOH.

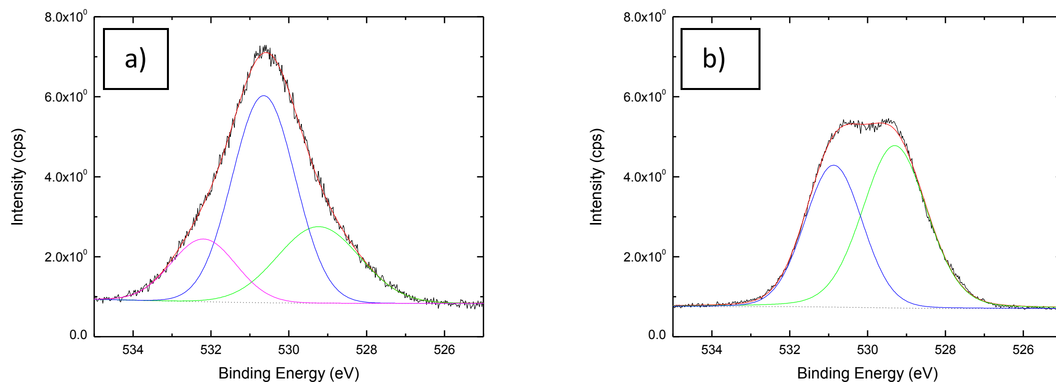

Figure 4.14 - The deconvoluted O 1s XPS spectra of YAG a) untreated b) treated with 30 minutes of NaOH

Figure 4.15 shows the high resolution Y 3d spectra for the YAG samples. For the untreated YAG the Y 3d lines have been deconvoluted into three peaks with energies of 156.3 eV, 158.2 eV, and 160.2 eV. The peak at 156.3 eV is associated with C-Y bonds due to contamination, the peak at 158.2 eV is associated with Y $3d_{5/2}$, and the peak at 160.2 eV is ascribed to Y $3d_{3/2}$ [75]. The NaOH treated spectra only has two peaks left, in which the peak intensity ratio between the Y $3d_{5/2}$ and Y $3d_{3/2}$ drops from 2.5 to 1.5 indicating yttrium bonds are also being broken during treatment. The carbon peak disappears in the treated sample indicating the contamination is removed by NaOH treatment

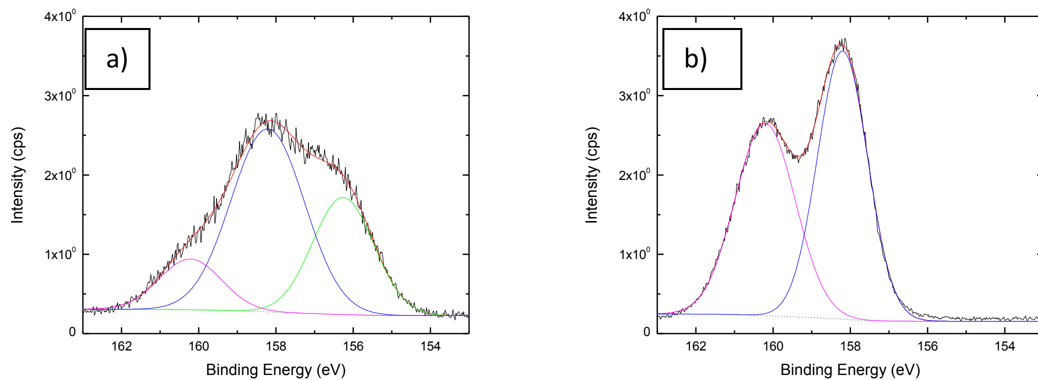

.

Figure 4.15 - The deconvoluted Y 3d XPS spectra of YAG a) untreated b) treated with 30 minutes of NaOH

With the preferential removal of the Al atoms from the surface of YAG, the surface begins to look more like Y_2O_3 in structure. Y_2O_3 has hardness values in literature as compared to YAG (Vicker's Hardness of 650 kg/mm2 vs 1700 kg/mm2) [70, 71]. The XPS spectra collected suggests that the NaOH solution selectively etches Al from the YAG surface and opens yttrium bonds, softening the surface which allows the SiO_2 slurry to mechanically abrade the modified surface material.

Chapter 5. CMP of Polycrystalline Y_2O_3

5.1. Introduction

In order to prepare the Y_2O_3 for wafer bonding experiments, the surfaces must meet the strict requirements for wafer bonding. The CMP process was developed to smooth the Y_2O_3 surface to acceptable values (< 1 nm RMS roughness), remove scratches from the surface, reduce subsurface damage from prior polishing steps, and maintain surface devoid of particles. The CMP processes were characterized by AFM and XRD and in order to understand the key steps in surface preparation.

5.2. Experimental Setup

12.5 mm polycrystalline Y_2O_3 substrates doped with Nd or Er were fabricated at Naval Air Weapons Station China Lake and used in all experiments. The polycrystalline Y_2O_3 samples required extra preparation steps prior to CMP to achieve desired surfaces, since the substrates did not begin with flat and parallel faces. The samples used in this experiment were first lapped by hand using a 20 μm SiC dispersion on a glass lapping plate to correct flatness and excessive RMS roughness (> 10 μm). The samples were then hand polished on a 6 μm diamond film then finished on 1 μm diamond film prior to CMP. The samples were attached to a carrier with wax surrounded by blanks to achieve uniform flatness, as seen in Figure 5.1.

Figure 5.1 – Mounting set up for polycrystalline Y_2O_3 polishing. The sample of interest is in the center

A Logitech PM5 CMP tool was used for all polishing and cleaning steps. The pads used in this study were a harder Suba 500 polishing pad and a softer Politex II polishing pad, with mechanical properties listed in Table 4.1. The slurries used in this experiment were a 70-nm SiO_2 suspension in a NaOH (4-6%) solution and a 70-nm Al_2O_3 suspension in a NaOCl (4-6%) solution. Samples were polished at 30 minute intervals with a slurry flow rate of 5 mL / min and rotational speed of 35 RPM with a constant pressure of 4 or 20 kPa.

After polishing, a 10 minute cleaning step was performed on the same tool to remove any abrasive particles from the surface. The pad used for the CMP step was then substituted with a pad that has not been exposed to slurry. Samples were then cleaned with two solutions kept separated prior to mixing on the pad: a solution with a NaOCl to water ratio of 1:10 and a solution with a citric acid ($C_6H_8O_7$) to water ratio of 1:2 for 5

minutes. A commercial surfactant, Rodelene, was then added to the pad and flushed with DI water for an additional 5 minutes. Pressure and rotation speed were maintained for the cleaning step. After cleaning, the surface morphologies (40 μm x 40 μm scans) were measured with atomic force microscopy (AFM) to determine suitability of sample for wafer bonding.

5.3. Al_2O_3 CMP Experimental Results

5.3.1 Surface Morphology Characterization of the CMP process

Initial Nomarski images (Figure 5.2) and profilometer scans (Figure 5.3) of Y_2O_3 substrates were taken prior to being subjected to CMP in order to determine the starting surface quality (roughness is out of range for AFM measurements at this point).

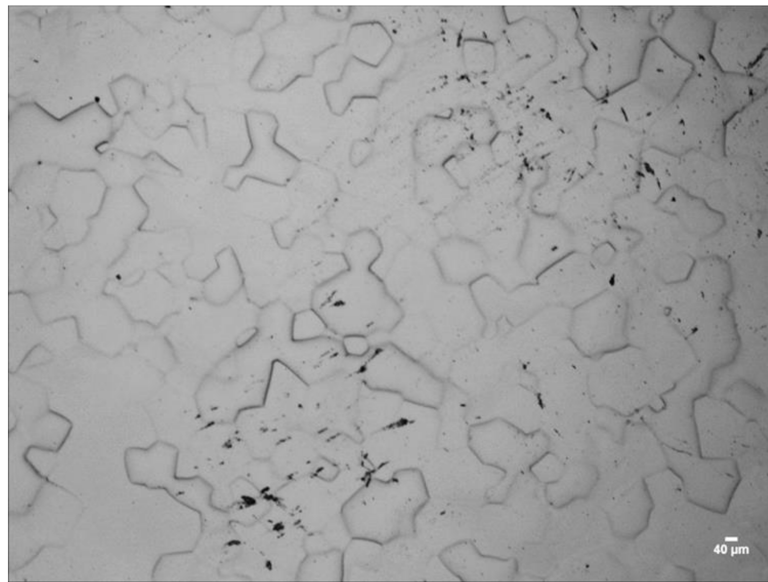

Figure 5.2 – Nomarski image for polycrystalline Y_2O_3 substrate as received, grain boundaries clearly present along with contamination of the surface.

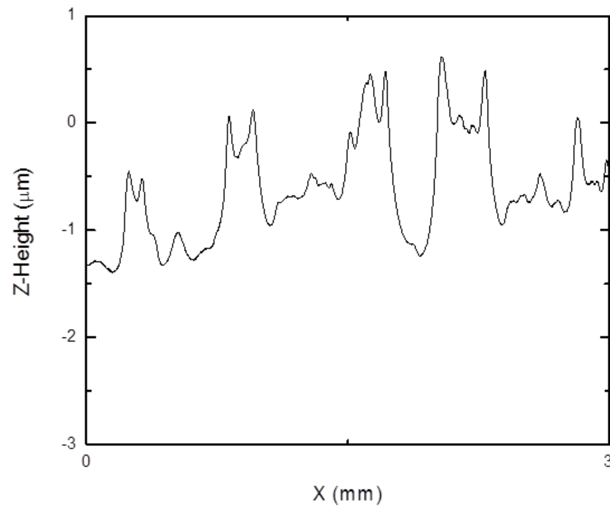

Figure 5.3 – Profilometer scan of the surface of polycrystalline Y_2O_3 substrate as received.

Figure 5.2 clearly shows the grain structure on the surface of the as-supplied Y_2O_3 substrates, with a radius of 100 – 200 μm. There is some form of contaminants on the surface as well, which show up as the black specks on the image. The profilometer line scan in Figure 5.3 shows the relative differences between the grain heights, in which there is a ~ ± 1 μm difference in heights between the grains. The RMS of the initial line scan was 0.79 μm, which is too large for wafer bonding. It is also too large for CMP, so grinding and lapping steps are required prior to CMP.

To remove the initial height differences, all samples were lapped with 20 μm SiC dispersion on a glass plate. Then they were further mechanically polished on a 6 and 1 μm diamond paper. The microscope image in Figure 5.4 shows the surface after this

treatment, revealing many scratches, but the grains and grain boundaries are no longer visible.

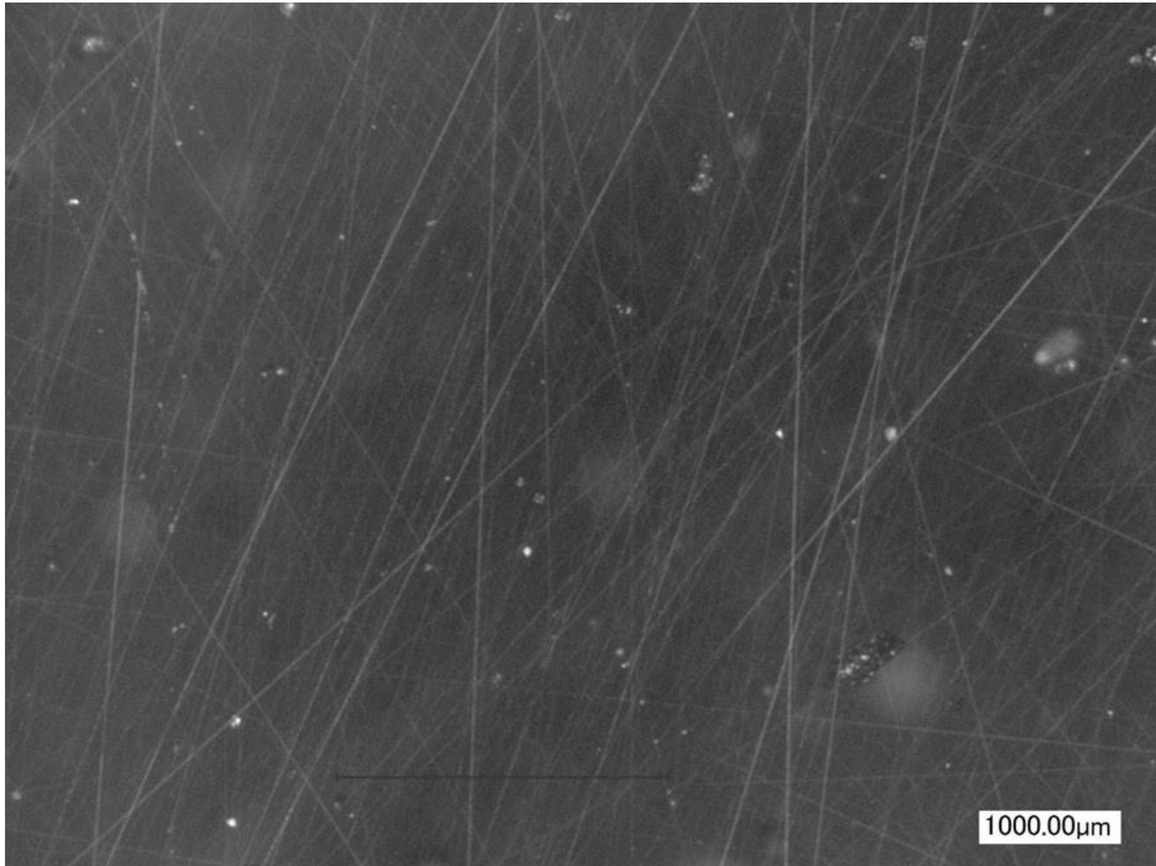

Figure 5.4 – Microscope image for polycrystalline Y_2O_3 substrate after mechanically grinding on 1 μm diamond paper , scratches are present.Futhermore, the profilometer line scan (Figure 5.5) of the Y_2O_3 surface shows that the scratches do not penetrate deeply into the sample. The RMS roughness of the line scan for the Y_2O_3 sample after mechanical diamond polishing is 6 nm, for reference a single crystal YAG sample was also measured to be 1-4 nm, as noted in Section 4.3.1. This shows that the initial

mechanical polishing is effective at flattening and 'smoothing' the substrate, such that CMP can be performed

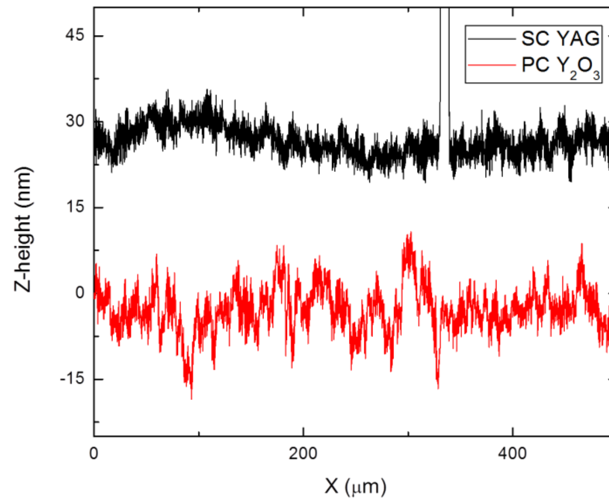

Figure 5.5 – Profilometer scan of the surface of polycrystalline Y_2O_3 substrate after mechanically polishing on 1 μm diamond paper, and a single crystal YAG sample (offset for clarity) for reference.

5.3.2 AFM Characterization of the CMP process

The initial surface preparation also is successful in reducing the area roughness enough to be in the range of AFM measurements. All substrates had 40 μm x 40 μm scans taken in 5 positions denoted by Figure 5.6 in order to detect non-uniformity during polishing.

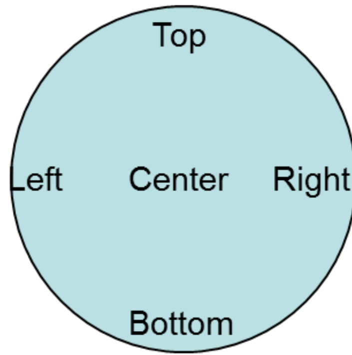

Figure 5.6 – Location of the AFM scan positions for each Y_2O_3 substrate

An example scan after mechanical polishing but prior to CMP is taken from the center position of an Y_2O_3 sample is shown in Figure 5.7, which shows the presence of scratches on the surface. The average RMS roughness values from the Y_2O_3 substrates prior to polishing were 10 – 20 nm.

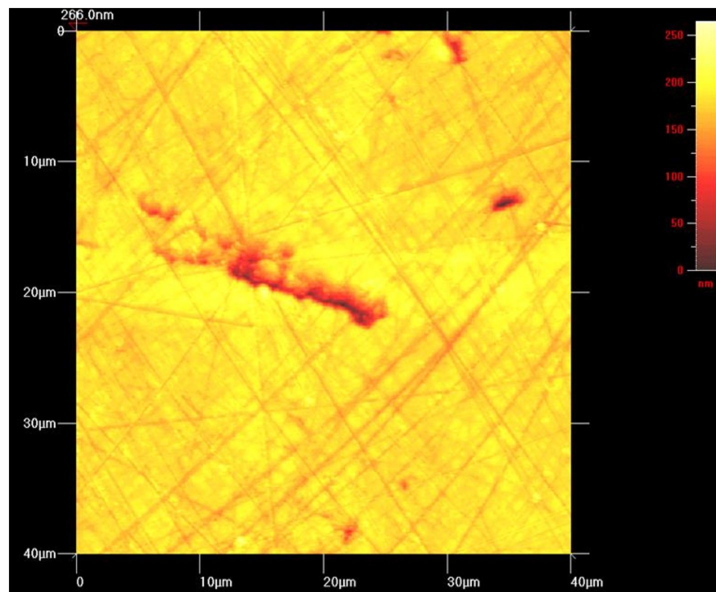

Figure 5.7 – 40 µm x 40 µm AFM scan at the center position for an Y_2O_3 substrate prior to CMP.

In Figure 5.7, the scan measures scratches 50 – 150 nm in depth. Initial AFM measurements showed that none of the samples received met the strict requirements of wafer bonding (< 1 nm RMS roughness and a particle-free surface) after this 1 μm mechanical diamond polishing step.

Once the samples were mechanically polished with diamond, the goal was to determine whether residual subsurface damage and scratches could be further removed via CMP. In order to CMP a polycrystalline material, careful consideration must be taken into account as the mechanical properties of the material to be polished (Y_2O_3) are a function of the orientation of the grains [57]. This means that without careful process control, over etching or over polishing of grains can easily occur and reduce the planarity of the surface. As shown below, it was found that the SiO_2/NaOH based slurry was very aggressive in etching the Y_2O_3 and promoted preferential polishing, so more focus was dedicated towards finding process conditions in which the Al_2O_3/NaOCl slurry could produce surfaces capable of wafer bonding.

The optical images in Figure 5.8 show how grains can be subjected to a preferential polish during CMP of the polycrystalline Y_2O_3 under various conditions, resulting in a non-uniform surface (except for Fig. 5.8b, which was subjected to the less chemically aggressive Al_2O_3/NaOCl slurry). Non-uniform removal rates can be attributed to the different grain orientations on the surface exhibiting different hardness or chemical-mechanical polishing rates [58]. Improved conditions were found in Figure 5.8b in which the removal rate of the grain and the intergrain materials are the same.

Achieving the planarization of this surface with CMP requires a high removal rate of the "high surface features" and a low/ negligible removal rate of the "low surface features". The difference in removal rates can be achieved on polishing pads that are more rigid and less compressible, such that the pad will not conform to the surface of the sample and the less force is applied to the "low features", leading to higher removal rates of the high features and lower removal rates of the low features [59].

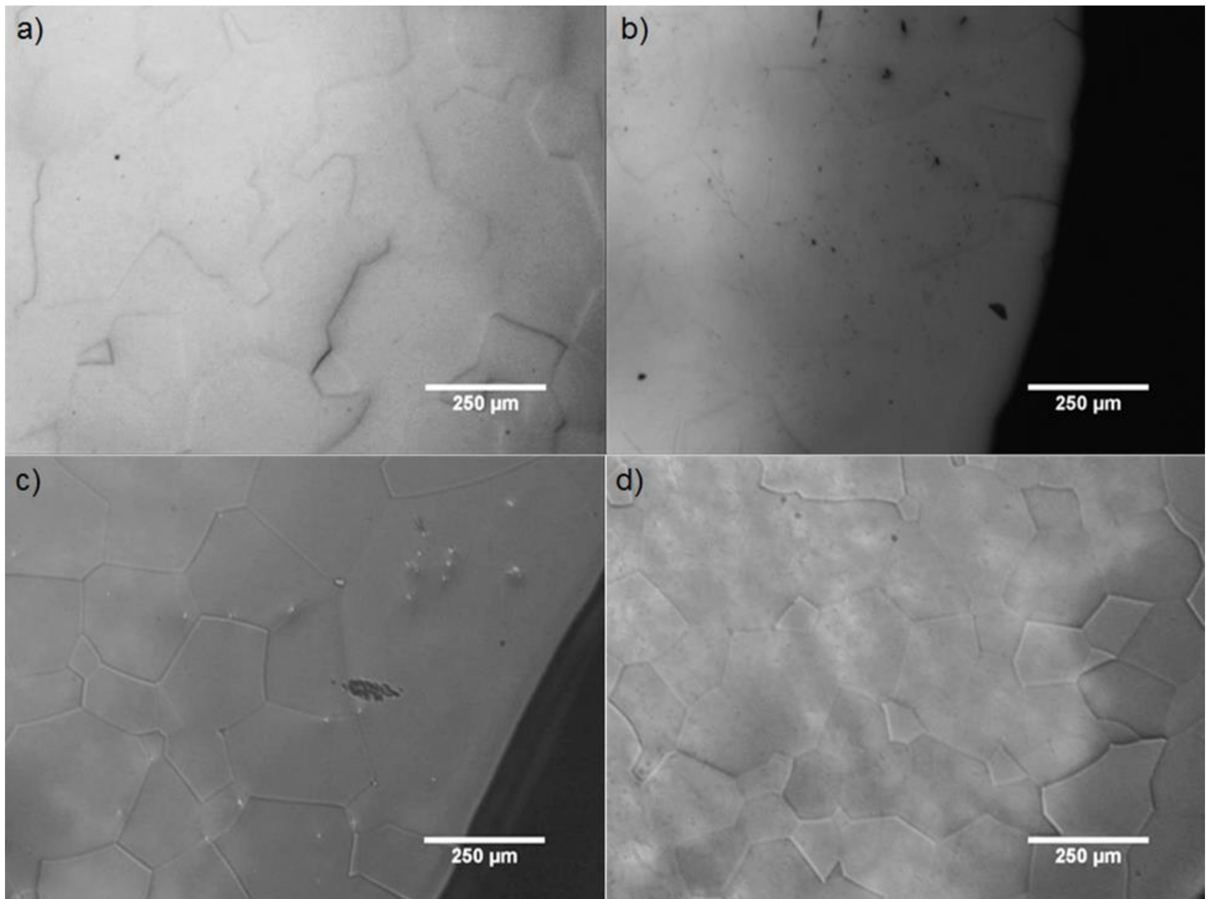

Figure 5.8 – Optical microscope images of CMP processing Y_2O_3 with various parameters: a) Pad: Suba 500, 4 kPa, b) Pad: Suba 500, 20 kPa, c) Pad: Politex, 4 kPa, d) Pad: Politex, 20 kPa

The AFM image in Figure 5.9 shows that the roughness after a 30 minute CMP with Al_2O_3/NaOCl of the Y_2O_3 sample. Initially, the Y_2O_3 had an RMS roughness of 16.0 nm with ~40 nm deep scratches, however after only 30 minutes of CMP the scratch depths have been reduced to ~ 1 nm and the RMS drops to 0.4 nm. The RMS roughness was measured by AFM on a total of 5 locations on the sample after each interval of polishing; the average RMS roughness is 0.5 nm after 30 minutes of Al_2O_3/NaOCl. The Y_2O_3 surfaces after the CMP and cleaning process are sufficiently smooth (< 1 nm RMS roughness) and particle free (< 1 particle / 1600 μm^2) to facilitate successful wafer bonding. Longer polishing times did not lower the scratch depth, and it was determined that surface was sufficient for wafer bonding experiments. However, further optimization of the polishing process should result in surfaces that are smooth and scratch free.

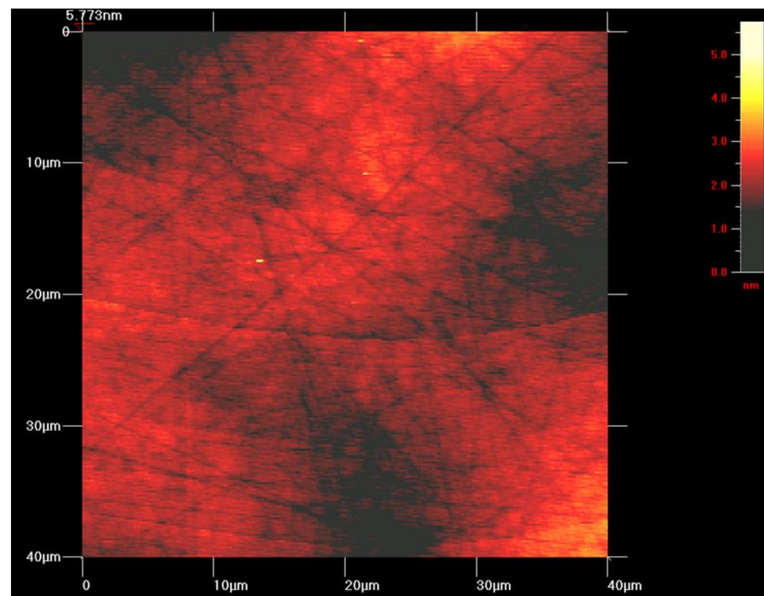

Figure 5.9 – 40 µm x 40 µm AFM scan at the center position for an Y_2O_3 after 30 minutes of Al_2O_3/NaOCl CMP

5.3.3 XRD Characterization of the CMP process

HRXRD was performed on the polycrystalline Y_2O_3 samples on a Bede D1 system before and after CMP, to detect any reduction of subsurface damage. This technique has been shown in limited applications but only using synchrotron sources [60, 61] and not for the study of subsurface damage in polycrystalline material. Using a lab x-ray source proved both insightful and useful in characterizing the polycrystalline sub-surface properties. Since the grains observed are ≥ 100 μm, the peak broadening due to grain size is minimal and the FWHM can be measured for individual grains. Figure 5.10 shows a double axis diffraction powder scan for Y_2O_3 in which the (222) peak of Y_2O_3 is highlighted after a 20 μm SiC lapping step

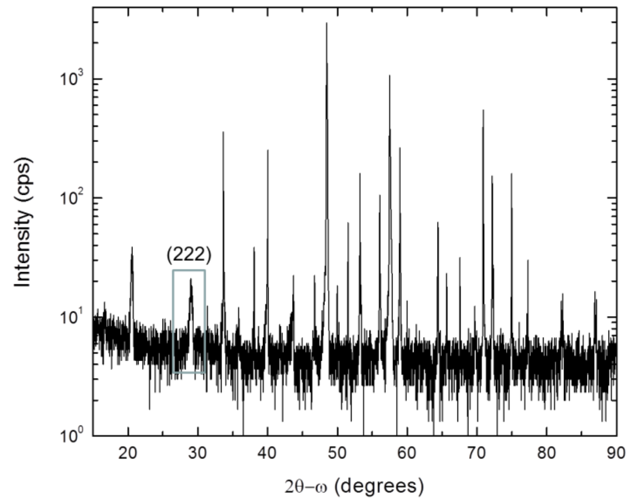

Figure 5.10 – Double crystal diffraction powder scan of polycrystalline Y_2O_3 after 20 μm SiC lapping.

A rocking curve (Figure 5.11) is then taken at the (222) position for Y_2O_3. Within this rocking curve, it is observed that there are multiple peaks each represents an individual grain whose (111) orientation is within a ±4.2° of the surface.

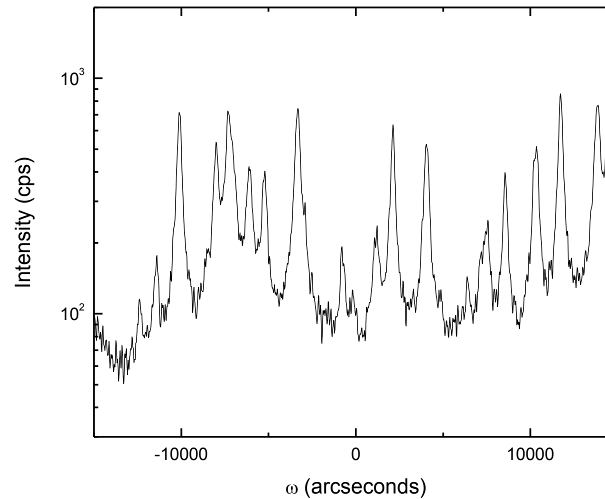

Figure 5.11 – Double crystal diffraction rocking curve of polycrystalline Y_2O_3 (222) after 20 μm SiC lapping.

Figure 5.12 was drawn to help illustrate what is occurring to produce this type of rocking curve. In this figure, the x-ray beam illuminates multiple large grains with different orientations, some of which have a (111) orientation that is almost parallel (within ±4.2°) with the sample surface. Small changes in the omega angle will satisfy Bragg's law for certain grains (the star indicates a grain in diffracting condition), and thus will produce multiple diffraction peaks as seen in the rocking curve, one peak for each grain that is correctly oriented.

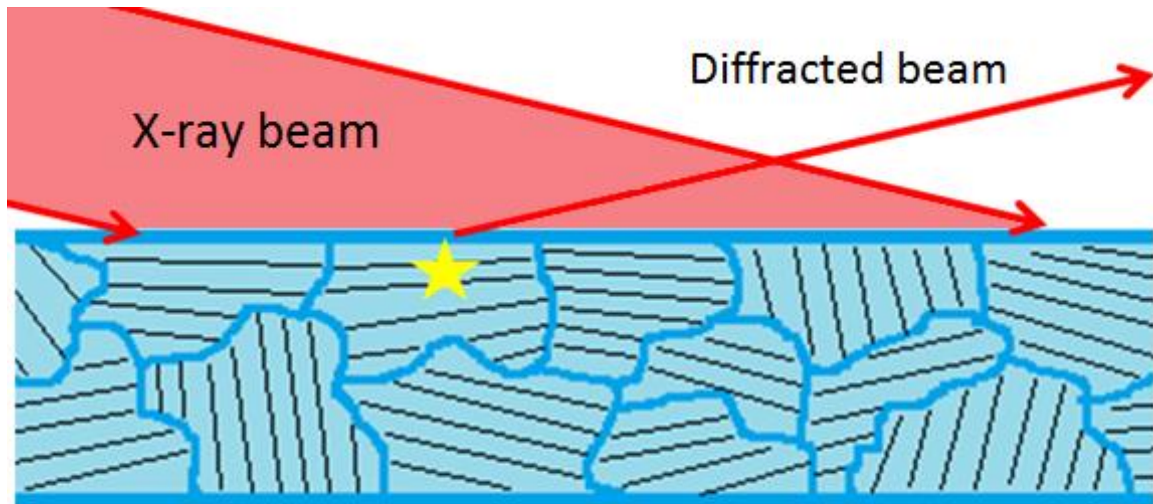

Figure 5.12 – Polycrystalline Surface with (222) planes drawn, incident X-ray beam illuminates multiple grains at once, but only the grain marked by the star is in a diffracting angle

Since the grains are very large, it is possible to optimize both the omega and chi angles for diffraction of each grain using triple axis diffraction (TAD). TAD rocking curves of the (222) plane for Y_2O_3 of individual grains were taken after each lapping and polishing step to determine if subsurface damage reduction was occurring. Figure 5.13 shows a set of rocking curves for each lapping/polishing step, along with fitted peaks to determine the FWHM.

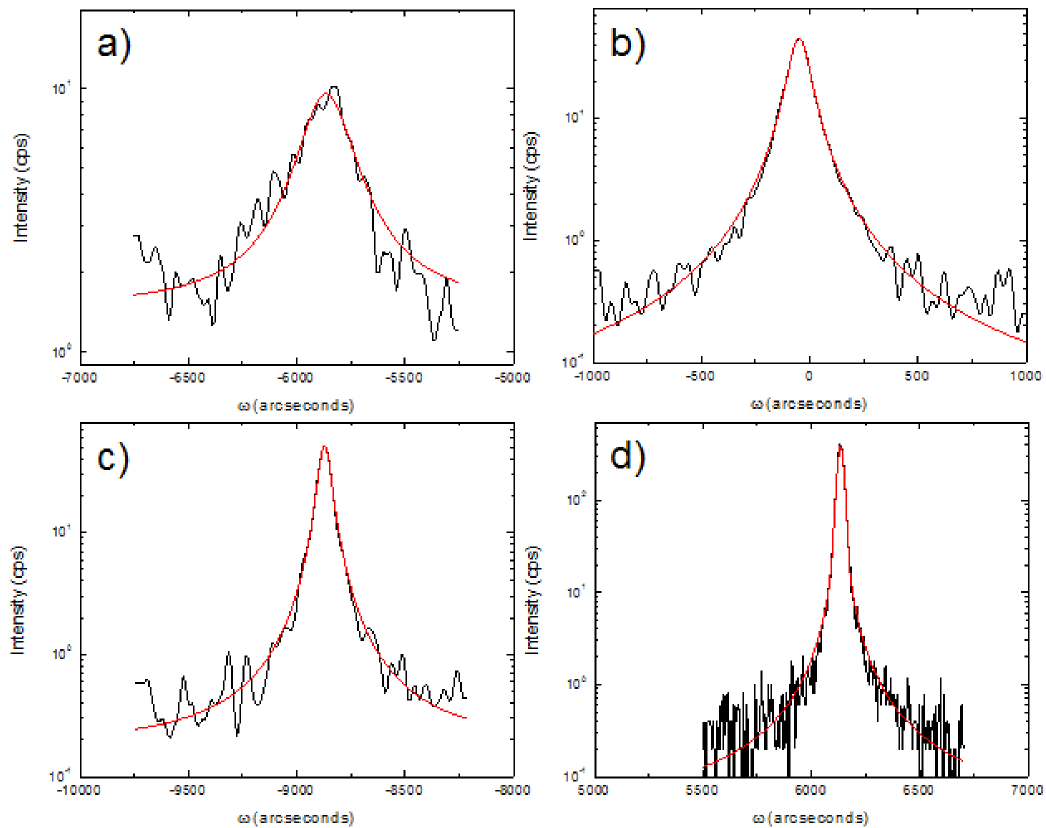

Figure 5.13 - TAD omega scans of Y_2O_3 (222) a) after 20 µm SiC lapping (FWHM 238") b) after 6 µm diamond lapping (FWHM 129") c) after 1 µm diamond lapping (FWHM 94") d) after Chemlox CMP FWHM(33")

Table 5.1 shows the compilation of FWHM for the Y_2O_3 samples after each step of lapping and polishing, and a reduction in FWHM is observed, indicating that even for polycrystalline samples that there is a significant amount residual subsurface damage that is removed by the CMP process (for this diffractometer the instrumental broadening is 15", which can be subtracted from the measured 33") . Note that these FWHM values are an average value of at least 5 different grains measured. The correlation between fracture

strength and subsurface damage has not yet been investigated in this study, but it is of interest for determining whether X-ray diffraction as non-destructive method to measure mechanical properties of these materials. It is noteworthy that the crystalline quality of the grains is improved with each subsequent polishing step, and can be used to further improve the processing of ceramic laser material for high power laser applications.

TABLE 5.1 Compilation of TAD rocking curve FWHMs

Grit	ω FWHM
20 μm SiC	238”
6 μm diamond	129”
1 μm diamond	94”
Chemlox	33”

Chapter 6. Microstructure Characterization of Bonded Structures

6.1. Introduction

In this chapter, bonding of the YAG and Y_2O_3 samples that underwent the CMP process is described. The ability to form a uniform bond across the entire sample surface is essential to the process of building laser composite elements that can be used for high power laser media. The thermomechanical strength must be able to withstand the temperature gradients without fracturing at the interface. The bonded interface must also have high transmissivity to maintain high lasing efficiencies. IR imaging measurements will be used to provide information about the bonding quality. It was found that CMP allowed surfaces to bond together at much lower temperatures than previously reported in literature. In addition, TEM provides images of the interface layer microstructure which found that after the high temperature annealing step there is direct crystalline contact between surfaces indicating a high quality bond has formed.

6.2. Experimental Setup

Bonding requires two smooth surfaces devoid of any large particles, which was achieved through the CMP process as discussed in Chapter 4 and 5. After the CMP process, the YAG (111) single crystal samples were prepared for bonding by acetone and IPA cleaning for 10 minutes each to remove any organic contamination. Samples were then rinsed in deionized water and dried with N_2. Samples were then subjected to an O_2 plasma (100 W) for 2 minutes to produce a hydrophilic surface [62]. Samples were then immersed into a dilute RCA1 solution prepared in a megasonic cleaner (1:1:100 ratio of

H_2O_2:NH_4OH:H_2O) for 5 minutes. Next, samples were rinsed in deionized water and dried with N_2. Samples were bonded by bringing the surfaces together and applying nominal pressure with tweezers. The samples were placed in an oven for a low temperature anneal at 250 °C for 24 hours, to evaporate and diffuse any water trapped at the interface. The samples were then placed in a tube furnace in air which was ramped to 1425 °C over a period of 12 hours, with temperature being held 1425 °C for 72 hours. No external force was used during the annealing steps.

6.3. Bonded Area

Initial bonding trials were successful at producing only small bonded areas (< 50%), despite maintaining a particle free surface and a smooth surface (< 4 Å RMS roughness) as seen in Figure 6.1. It was thought that the small bonding area was caused by poor flatness of the samples, which is later addressed.

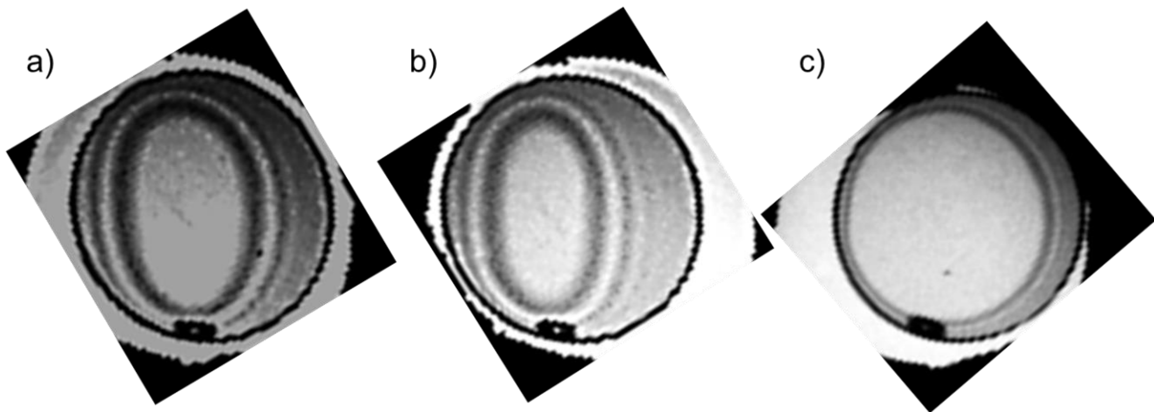

Figure 6.1 – IR Images of YAG/YAG bonding (10 mm diameter) a) as bonded (room temp), b) annealed at 250 °C for 24 hours, c) annealed at 1425 °C for 72 hours

The sample in Figure 6.1 has a bonding area % of 26% → 19% → 68% after each respective heat treatment. The bonding area first decreases and then ultimately increases by a large amount from the higher temperature anneal. The increase in bonding area may be attributed to as the sample is heated up, the surfaces are expanding and are forced into contact with each other resulting in a stronger bond. However, this is still not desirable results, as initial bonding should occur over the entire surface of the sample given a flat, smooth, and clean surface. It was determined that the lapping and polishing procedures, were having a rounding effect in which the surfaces were losing their flatness. By adjusting the polishing mounting scheme as seen in Figure 5.1, the bonding area rose to 90% at all stages of post bonding annealing as seen in Figure 6.2.

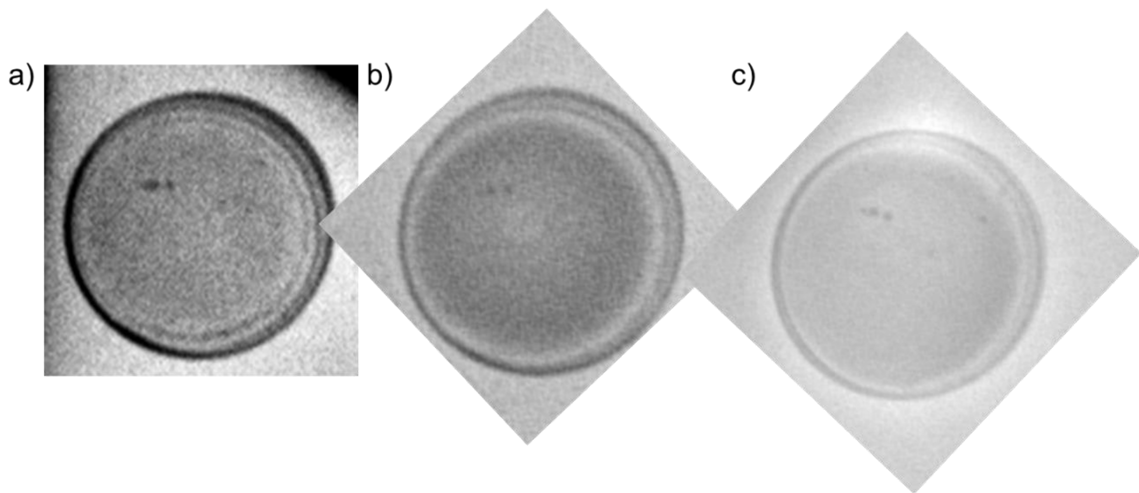

Figure 6.2 – IR Images of YAG/YAG bonding (10 mm diameter) with optimized polishing process (90% area bonded) a) as bonded (room temp), b) annealed at 250 °C for 24 hours, c) annealed at 1425 °C for 72 hours

Polycrystalline Y_2O_3 bonding was also achieved using the same processes and techniques and can be seen in Figure 6.3. The image clarity is not as good, because the surfaces of the as-received wafers are rough as noted before and only the surface that was used for bonding was polished using CMP.

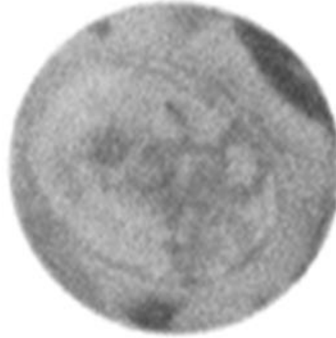

Figure 6.3 – IR Image of Y_2O_3/Y_2O_3 bonding (10 mm diameter) with optimized polishing process after annealing at 1425 °C for 72 hours

The maximum bonded area of the Y_2O_3/Y_2O_3 sample was only 50%, which is attributed towards incomplete process optimization of the lapping and CMP step, in which the flatness can still be improved.

6.4. Interface Microstructure

To investigate the bonding quality and the microstructure of the interface, HRTEM was used to image the cross section and the plan view specimens of the YAG/YAG interface that was annealed at 1425 °C for 72 hours. Figure 6.4 shows a HRTEM image of the bonding interface.

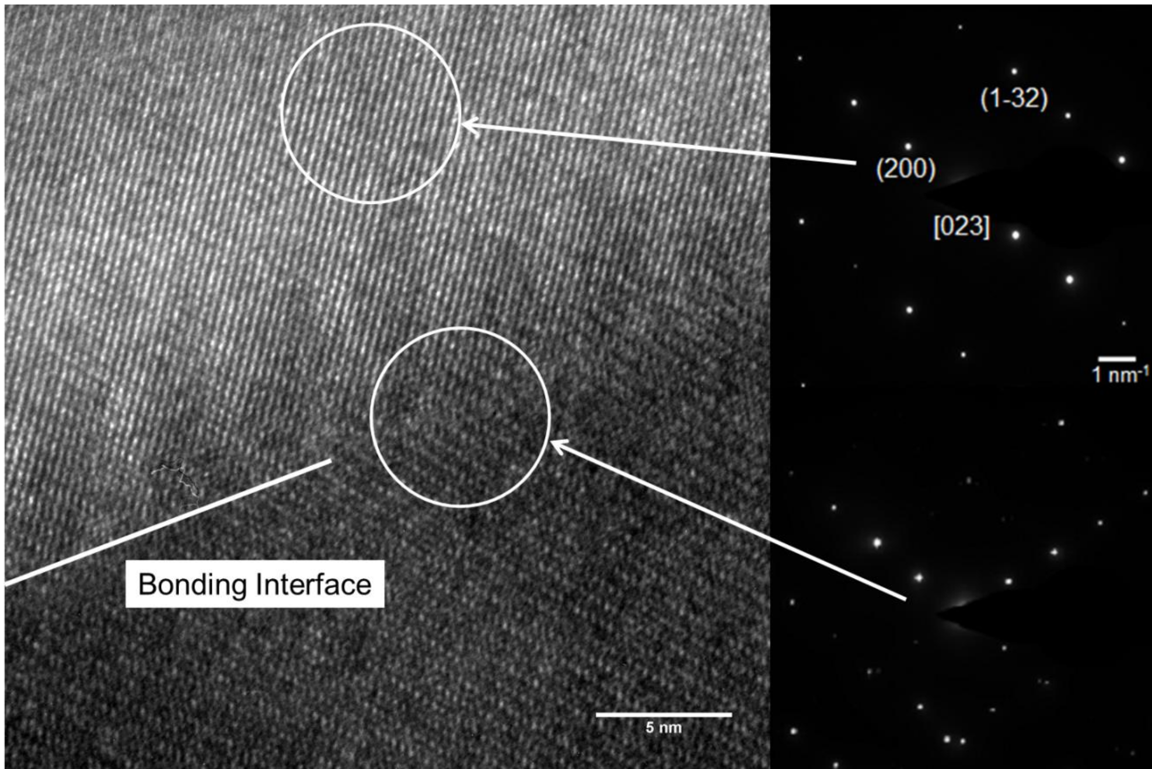

Figure 6.4 – Cross section of bonded YAG/YAG interface after annealing. [023] Zone Axis.

The cross section image is aligned to the [023] zone axis and gives atomic resolution of the bonded interface. Diffraction patterns were also taken from the top wafer and from the bonded region, to observe whether any interfacial layers exist. The atomic resolution obtained from both wafers combined with slight deviations of the diffraction patterns, indicate that the wafers were bonded with a $< 3°$ twist. The presence of well fused crystalline regions is indicated by continuous lattice fringes of both crystals at the interface and matching single crystal diffraction patterns. No thin intermediate layers or defect features were found at the interface which could act as potential scattering sites. This shows the potential for CMP and wafer bonding to be used to a create composite

laser elements with minimal loss in optical quality. In addition the lack of these interstices shows a bond that has potential for greater thermomechanical properties, which is an important element for high power lasing applications [33]. Plan view images of the same sample were taken as seen in Figure 6.5 to capture a greater area of the bonded interface (~25 μm^2). Again no defects were observed in the plan view images under various bright field and dark field conditions indicating high quality bonds were achieved at lower temperatures and pressures (1425 °C and no applied pressure) than has previously been reported in literature (~1550-1700 °C and ~100 kPa) [30]. The improvements shown in this study demonstrate the effectiveness of the CMP process for fabrication of future high powered SSL composite laser elements.

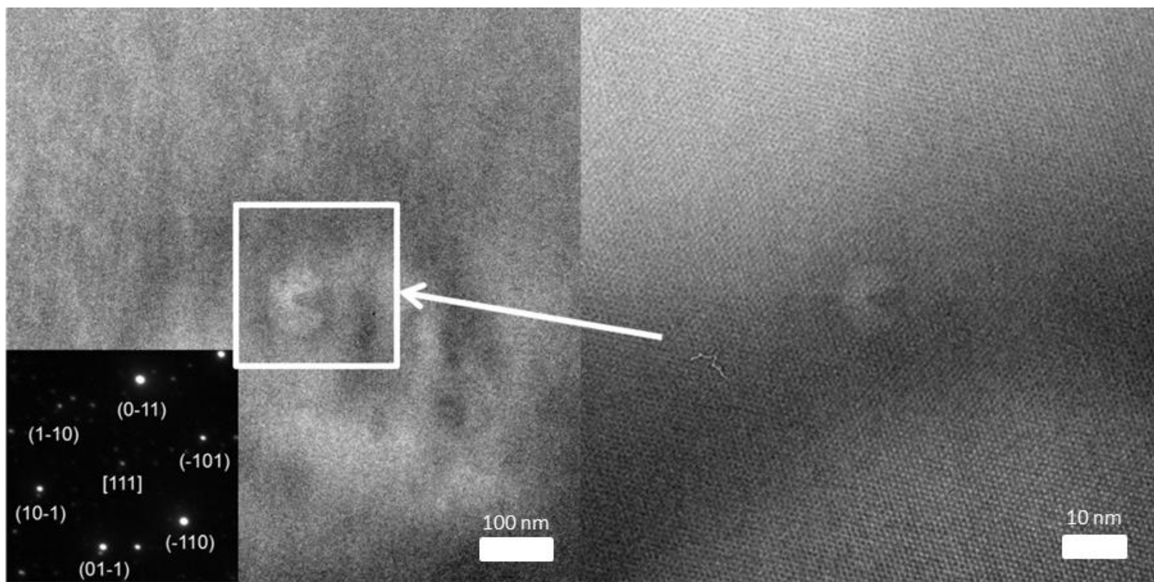

Figure 6.5 – Plan view of bonded YAG/YAG interface after annealing. [111] Zone Axis.

Chapter 7. Future Work

7.1. Summary

In this study, first CMP was performed on YAG and Y_2O_3 substrates in order to reduce the amount of subsurface damage and to smooth the surfaces such that they can be subsequently wafer bonded. The sample surfaces were characterized with AFM, XRD, XPS, and optical microscopy to guide the CMP process in producing the best possible surface finish. It was determined that CMP provides additional benefits over conventional polishing methods, such as the removal of fine scratches and reduction in subsurface damage. This shows the necessity in CMP for producing high quality lasing material.

When surfaces met the requirements for wafer bonding, they were then subjected to various chemical treatments to enhance the wettability of the surface to promote hydrophilic bonding. Once the samples were bonded, they underwent heat treatments to further strengthen and solidify the bonds. The bonded interface of YAG/YAG was examined by HRTEM which determined the bonding quality of the interface was continuous well fused crystalline regions with no observable defects, indicating that this technique is promising for further developments of the bonding of YAG/YAG and Y_2O_3/Y_2O_3 for high power laser composite element applications.

7.2. Y_2O_3/Y_2O_3 Bonding Interface Characterization

It would be of interest to reproduce the Y_2O_3/Y_2O_3 sample and produce a TEM cross section and plan view samples to observe the microstructure of a polycrystalline

bonded sample. This will help show the interfacial microstructure of the high quality bonding that is achieved for the polycrystalline samples.

7.3. Bond Strength Characterization

YAG/YAG and Y_2O_3/Y_2O_3 samples were successfully bonded together via the processes outlined above. However the bonding strength of the samples was not yet measured. The bonding strength will play a crucial aspect in the amount of power that can be put into any lasing element as the fracture points typically occur at the bonded interface for current composite laser elements. Being able to produce a composite laser element with a bonding strength near or equal to the bond strength of the starting material would allow for high power laser applications to be realized.

7.4. Optical Transmission Characterization

The next important aspect is the optical transmission characteristics of the bonded interface. The bonded interface should ideally be free from defects, thus have no efficiency loss due to scattering when the laser passes through it. The optical transmission is a critical aspect to determining whether the bonding can be successfully used to produce composite laser elements using the aforementioned CMP and bonding processes.

7.5. Heat Transfer Characterization

Current composite laser elements still have poor thermomechanical properties due to interstices that are formed at the interface. These interstices impede the heat transfer, and thus the elements are not resistant to high power laser damage. Testing the thermomechanical properties of the bonds produced in this study will help determine the

feasibility and modifications that must be made to the process in order to realize a fully functioning high power laser element.

Bibliography

1. W. Koechner, *Solid-State Laser Engineering*, Vol. 1, Springer, Berlin (2006): 1-10.

2. J. E. Geusic, H. M. Marcos, and L. G. van Uitert. Applied Physics Letters 4, no. 10 (1964): 182-184.

3. B. P. Abbott, Reports on Progress in Physics 72, no. 7 (2009): 076901.

4. C. Block, J. Mayo, and G. Evans, The International Journal of Oral & Maxillofacial Implants 7, no. 4 (1991): 441-449.

5. J. White, H. Goodis, and C. Rose, Lasers in Surgery and Medicine 11, no. 5 (1991): 455-461.

6. M. Kavaya, Optics Letters 14, no. 15 (1989): 776-778.

7. D. Winker, W. Hunt, and C. Hostetler, Remote Sensing (2004)

8. I. Almeida, Journal of Materials Processing Technology 179, no. 1 (2006): 105-110.

9. S. Sun, Y. Durandet, and M. Brandt, Surface and Coatings Technology 194, no. 2 (2005): 225-231.

10. N. Basov, Drivers for Inertial Confinement Fusion (1995)

11. W. Steen, K. Watkins, and J. Mazumder, *Laser Material Processing*, Springer, London (2010): 51-76.

12. R. Weber, B. Neuenschwander, and H. Weber, Optical Materials 11, no. 2 (1999): 245-254.

13. T. Kane and R. Byer, Optics Letters 10, no. 2 (1985): 65-67.

14. W. Koechner, *Solid State Engineering*, Springer, Verlag (1976) 32-73.

15. R. Monchamp, Journal of Crystal Growth 11, no. 3 (1971): 310-312.

16. M. Umino and M. Abe, Optronics Magazine 40 (1985): 93-97.

17. Y. Peizhi, Journal of Crystal Growth 218, no. 1 (2000): 87-92.

18. E. Sabisky and C. Anderson, Physical Review Letters 13, no. 25 (1964): 754-755.

19. A. Ikesue, Journal of the American Ceramic Society 78, no. 4 (1995): 1033-1040.

20. H. Hoskins and B. Soffer, Applied Physics Letters 4 (1963): 22-23.

21. J. Stone and C. Burrus, Journal of Applied Physics 49 (1978): 2281-2287.

22. A. Diening, B. Dicks, E. Heumann, J. Meyn, K. Petermann and G. Huber, Advanced Solid-State Lasers 10 (1997): 194-196.

23. A. Kaminskii, *Laser Crystal, Their Physics and Properties*, Springer, Berlin (1990).

24. P. Klein and W. Croft, Journal of Applied Physics 38 (1967): 1603-1607.

25. J. Lu, Jianren, Japanese Journal of Applied Physics 40, no. 12A (2001): L1277-L1279.

26. J. Lu, T. Murai, K. Takaichi, T. Uematsu, K. Misawa, M. Prabhu, J. Xu, K. Ueda, H. Yagi, T. Yanagitani, A. Kaminskii and A. Kudryashov, Applied Physics Letters 78 (2001): 3586-3587.

27. J. Stone and C. Burrus, Journal of Applied Physics 49, no. 4 (1978): 2281-2287.

28. E. Kannatey-Asibu Jr, *Principles of Laser Materials Processing,* Vol. 4, John Wiley & Sons, Hoboken (2009): 135-180.

29. A. Ikesue and Y. Aung, Nature Photonics 2, no. 12 (2008): 721-727.

30. H. Lee, Laser-Induced Damage in Optical Materials 1624 (1991): 1-11.

31. K. Hartmann, R. Wirth, and W. Heinrich, Physics and Chemistry of Minerals 37, no. 5 (2010): 291-300.

32. A. Ikesue, Annual Review of Materials Research 36 (2006): 397-429.

33. A. Ikesue, Y. Aung, and V. Lupei, *Ceramic Lasers*, Cambridge University Press, Cambridge (2013).

34. M. Oliver, *Chemical-Mechanical Planarization of Semiconductor Materials*, Vol. 69, Springer, New York (2013).

35. F. Preston, Transactions of the Optical Society 27, no. 3 (1926): 181-190.

36. F. Shi and B. Zhao, Applied Physics A: Materials Science & Processing 67, no. 2 (1998): 249-252.

37. Q. Luo, S. Ramarajan, and S. Babu, Thin Solid Films 335, no. 1 (1998): 160-167.

38. C. Liu and Chi-Wen, Journal of the Electrochemical Society 143, no. 2 (1996): 716-721.

39. Q. Tong and U. Goesele, *Semiconductor Wafer Bonding: Science and Technology*, John Wiley, New York (1999).

41. M. Kobayashi, Langmuir 21, no. 13 (2005): 5761-5769.

42. R. Stengl, T. Tan, and U. Gösele, Japanese Journal of Applied Physics 28, no. 10R (1989): 1735-1741.

43. W. Maszara, Journal of Applied Physics 64, no. 10 (1988): 4943-4950.

44. M. Shimbo, Journal of Applied Physics 60, no. 8 (1986): 2987-2989.

45. T. Suni, Journal of the Electrochemical Society 149, no. 6 (2002): G348-G351.

46. D. Lessor, J. Hartman, and R. Gordon, Journal of the Optical Society of America 69, no. 2 (1979): 357-366.

47. H. Yoon, S. Lindo, and M. Goorsky, Journal of Crystal Growth 174, no. 1 (1997): 775-782.

48. C. Reyner, Applied Physics Letters 99, no. 23 (2011): 231906.

49. S. Hayashi, T. Koga, and M. Goorsky, Journal of the Electrochemical Society 155, no. 2 (2008): H113-H116

50. S. Hayashi, M. Joshi, and M. Goorsky, ECS Transactions 16, no. 8 (2008): 295-302.

51. C. Wagner, "NIST X-ray Photoelectron Spectroscopy Database (Version 2.0)." (1997)

52. D. Briggs and M. Seah, *Practical Surface Analysis by Auger and X-ray Photoelectron Spectroscopy*, John Wiley & Sons, Chichester (1983)

53. M. Schmidt, Proceedings of the IEEE 86, no. 8 (1998): 1575-1585.

54. A. Rosenauer, Optik 102, no. 2 (1996): 63-69.

55. J. Steigerwald, S. Murarka, and R. Gutmann, *Chemical Mechanical Planarization of Microelectronic Materials*, John Wiley & Sons, New York (2008)

56. M. Bachman, INRF Application Note Engineering of Microworld at the University of California. Irvine (1999)

57. D. Lee, D. Kim, and D. Cho, Journal of Materials Science Letters 17, no. 3 (1998): 185-187.

58. S. Yi, J. Cho, and J. Park, Journal of the Electrochemical Society 159, no. 11 (2012): C546-C551

59. L. Zhang, S. Raghavan, and M. Weling, Journal of Vacuum Science & Technology B 17, no. 5 (1999): 2248-2255.

60. P. Withers and P. Webster, Strain 37, no. 1 (2001): 19-33.

61. M. Golshan, D. Landry, P. Fewster, M. Moore, A. Whitehead, J.E. Butler, and O. Konovalov, Journal of Physics D: Applied Physics 36 (2003): A153-A156.

62. S. Hayashi, Journal of Physics D: Applied Physics 38, no. 10A (2005): A174-A178.

63. A. Ikesue and Y. Aung, Journal of American Ceramic Society 89, no. 6 (2006): 1936-1944.

64. X. Wang, Z. Zhao, X. Wu, J. Wang, J. Xu, B. Gilbet, and J. Chanteloup, Science in China Series E: Technological Sciences 51, no. 9 (2008): 1457-1463.

65. L. Jun, Y. Zhu, and C. Chen, Key Engineering Materials 375 (2008): 278-282.

66. J. Emmett, W. Krupke, and J. Trenholme, Soviet Journal of Quantum Electronics 13, no. 1 (1983): 1-23.

67. V. Wang and R. Matyi, Journal of Applied Physics 72 (1992): 5158-5164.

68. C. Moore, I. Pape, and B. Tanner, Nuovo Cimento Societa Italiana di Fisica D 19 (1997): 205-212.

69. R. Köhler, Applied Physics A 58, no. 3 (1994): 149-157.

70. J. Cha, S. Hwang, and E. Lee, Journal of Mechanical Science and Technology 23, no 4. (2009): 1194-1201.

71. D. Sirdeshmukh, L,Sirdeshmukh, and K. Subhadra, *Micro-and Macro-Properties of Solids*, Springer, Berlin (2006): 172.

72. D. Camp, Laser-Induced Damage in Optical Materials 3244 (1997): 356-364.

73. W. Lee, S. Kim, Y. Seo, J. Lee, Journal of Materials Science: Materials in Electronics 12 (2001): 63-68.

74. Y. Seo and S. Kim, Japan. Journal of Applied Physics 41 (2002): 6310-6312.

75. M. Kruczeka, Acta Physica Polonica A 115, no. 1 (2009): 209-212.

76. J. Shen, Optik-International Journal for Light and Electron Optics 116, no. 6 (2005): 288-294.

77. J. Marion, Applied Physics Letters 47, no. 7 (1985): 694-696.

78. D. Pawlak, The Journal of Physical Chemistry B 103, no. 9 (1999): 1454-1461.

79. M. Kruczek, Crystal Research and Technology 40, no. 4-5 (2005): 439-443.

80. M. Jackson, Journal of Electronic Materials 40, no. 1 (2011): 1-5.